

INVESTIGATION OF THE FLEXIBLE MISSILE FINS
UNDER AEROTHERMAL LOADING

A THESIS SUBMITTED TO
THE GRADUATE SCHOOL OF NATURAL AND APPLIED SCIENCES
OF
MIDDLE EAST TECHNICAL UNIVERSITY

BY

EMİR ÖZKÖKDEMİR

IN PARTIAL FULFILLMENT OF THE REQUIREMENTS
FOR
THE DEGREE OF MASTER OF SCIENCE
IN
AEROSPACE ENGINEERING

JUNE 2018

Approval of the thesis:

**INVESTIGATION OF THE FLEXIBLE MISSILE FINS
UNDER AEROTHERMAL LOADING**

submitted by **EMİR ÖZKÖKDEMİR** in partial fulfillment of the requirements for the degree of **Master of Science in Aerospace Engineering Department, Middle East Technical University** by,

Prof. Dr. Halil Kalıpçılar
Dean, Graduate School of **Natural and Applied Sciences**

Prof. Dr. Ozan Tekinalp
Head of Department, **Aerospace Engineering**

Assoc. Prof. Dr. Dilek Funda Kurtuluş
Supervisor, **Aerospace Engineering Dept., METU**

Examining Committee Members:

Prof. Dr. Yusuf Özyörük
Aerospace Engineering Dept., METU

Assoc. Prof. Dr. Dilek Funda Kurtuluş
Aerospace Engineering Dept., METU

Prof. Dr. Altan Kayran
Aerospace Engineering Dept., METU

Prof. Dr. Şenol Başkaya
Mechanical Engineering Dept., Gazi University

Assoc. Prof. Dr. Demirkan Çöker
Aerospace Engineering Dept., METU

Date: 21.06.2018

I hereby declare that all information in this document has been obtained and presented in accordance with academic rules and ethical conduct. I also declare that, as required by these rules and conduct, I have fully cited and referenced all material and results that are not original to this work.

Name, Last name : Emir Özkökdemir

Signature :

ABSTRACT

INVESTIGATION OF THE FLEXIBLE MISSILE FINS UNDER AEROTHERMAL LOADINGS

Özkökdemir, Emir

MSc., Department of Aerospace Engineering

Supervisor: Assoc. Prof. Dr. Dilek Funda Kurtulus

June 2018, 80 pages

Wings or fins on the body flying at the supersonic speed are subjected to the aerothermal loading. These loads are categorized into two main groups; aerodynamic pressure and aerodynamic heating. They affect the strength of wings. In this thesis study, a flexible NACA 65-009 wing of a missile flying at supersonic speed is investigated. It is studied to define the effect of the change in wing geometry by the external loads on the flow characteristics. The flow simulations are carried on Ansys Fluent that uses the finite-volume method with the SIMPLE-type fully implicit algorithm to solve the conservation equations. Abaqus Standard is used for simulating the load cases to obtain the structural deformation by using the finite element technique. According to the result of simulations, the effect of deformation at lower supersonic regime ($1.2 < M < 2$) is relatively lower but it becomes important when the free stream velocity reaches to Mach number of 2.5 and the difference of aerodynamic performances (drag coefficients) of deformed and undeformed wings is about 8.6 %.

Keywords: Aero-Thermal Wing Deformation, Thermo-Mechanic, Computational Fluid Dynamic, Finite Element Methods

ÖZ

AEROTERMAL YÜKLER ALTINDA ESNEK FÜZE KANATLARININ İNCELENMESİ

Özkökdemir, Emir

Yüksek Lisans, Havacılık ve Uzay Mühendisliği Bölümü

Tez Yöneticisi: Doç. Dr. Dilek Funda Kurtuluş

Haziran 2018, 80 sayfa

Süpersonik hızlarda uçan yapılarda bulunan kanatlar aerotermal yüklere maruz kalırlar; Bu yükler aerodinamik basınç ve aerodinamik ısınma olmak üzere iki gruba ayrılırlar. Her ikisi de kanat dayanımının üzerinde etkilidir. Bu tez çalışmasında, bir füze için esnek bir NACA 65-009 kanadı süpersonik akış koşulları altında incelenmiştir. Kanadın yapısında görülen bozulmaların akış koşullarına nasıl etki ettiği belirlenmiştir. Akış simülasyonları, SIMPLE-tipi kapalı algoritma ile sonlu hacimler yöntemi kullanarak korunum denklemlerini çözen Ansys Fluent yazılımı ile gerçekleştirilmiştir. Abaqus Standard ile sonlu elemanlar yöntemi kullanarak yükleme durumları simüle edilmiş ve yapısal deformasyon hesap edilmiştir. Bu çalışma kapsamında yapılan simülasyonlardan elde edilen sonuçlara göre, düşük süpersonik rejimde ($1.2 < M < 2$) deformasyonun etkisi oldukça azdır. Fakat akış hızı 2.5 Mach seviyelerine ulaştığında bu etki daha önemli olmaktadır. Deforme olmuş ve olmamış kanatların aerodinamik performansları (sürükleme katsayıları) arasındaki fark % 8.6'dır.

Anahtar Sözcükler: Aero-Termal Kanat Deformasyonu, Termomekanik, Hesaplamalı Akışkanlar Dinamiği, Sonlu Elemanlar Yöntemi

To My Family

ACKNOWLEDGMENTS

The author would like to thank to Assoc. Prof. Dr. D. Funda Kurtuluş for her supervision and understanding.

The author would also like to thank to Bülent Acar and Emre Kütükçeken for their crucial suggestions and supports and sharing their experiences and ROKETSAN for supporting to the test facilities in this thesis study.

The author specially would like to thank to his wife Ezgi Özkökdemir and his family; Timur and Aysel Özkökdemir for their encouragements and endless support during the period of this thesis study.

TABLE OF CONTENTS

ABSTRACT	v
ÖZ	vi
ACKNOWLEDGMENTS.....	viii
TABLE OF CONTENTS	ix
LIST OF TABLES	xi
LIST OF FIGURES	xii
CHAPTERS	
1. INTRODUCTION	1
1.1. Deformation Phenomena	3
1.2. Literature Survey	4
1.3. Motivation	8
2. METHODOLOGY	11
2.1. Basic Definitions	11
2.2. Procedure of the Method	18
3. VALIDATION STUDIES	21
3.1. Simulation Models	21
3.1.1. CFD Simulation Models	23
3.1.2. FE Simulation Models	25
3.2. Grid Refinement Study	27
3.2.1. Grid Refinement for the CFD Simulations	27
3.2.2. Grid Refinement for the FE Simulations	32
3.3. Turbulence Models	34
4. RESULTS OF THE NUMERICAL SIMULATIONS.....	37
4.1. Simulations for the 2D NACA 65-009 Airfoil	37
4.2. Simulations for the 3D NACA 65-009 Wing	45
4.3. Simulations for the Missile Equipped with 3D NACA65-009 Wing.....	56
5. CONCLUSION	69
REFERENCES.....	71

APPENDICES

A. MATERIAL CHARACTERIZATION TESTS 75

LIST OF TABLES

TABLES

Table 1. Classification of missiles	1
Table 2. Mechanical and thermal properties of aluminum 2000 series	27
Table 3. Grid refinement study for the CFD simulations.....	28
Table 4. Grid refinement study for the FE simulations.....	33
Table 5. Grid refinement study for FE simulations.....	34
Table 6. Deformations on wing body for different Mach number	52
Table 7. Wing drag coefficient (C_D) for deformed and undeformed wing	55
Table 8. Deformations on the wing body for different Mach number	64
Table 9. Wing drag coefficient (C_D) for deformed and undeformed wing - 2.....	65

LIST OF FIGURES

FIGURES

Figure 1. Canards, wings and tail fins	2
Figure 2. Resultant aerodynamic force and the components	11
Figure 3. Velocity and temperature profile inside the boundary layer.....	13
Figure 4. Control volume	14
Figure 5. Stresses on a finite element.....	16
Figure 6. Procedure of the method	20
Figure 7. NACA 65-009 airfoil	21
Figure 8. Flight test model by the Langley Laboratory, by Alexander (1947)	22
Figure 9. Two-dimensional flow domain and boundary conditions	23
Figure 10. Three-dimensional flow domain and boundary conditions	23
Figure 11. FE simulation of the clean wing configuration.....	26
Figure 12. FE simulation of the full model configuration.....	26
Figure 13. Element types used in the CFD simulations	28
Figure 14. Grid levels for the 2D flow simulations.....	29
Figure 15. Grid levels for 3D flow simulations	29
Figure 16. Total drag coefficient of airfoil for different meshes	30
Figure 17. Pressure and viscous drag coefficient of airfoil for different meshes.....	30
Figure 18. Total drag coefficient of wing for different meshes	31
Figure 19. Pressure and viscous drag coefficient of wing for different meshes	31
Figure 20. 3D stress elements for FE simulations.....	32
Figure 21. Grid levels for the FE simulations of the clean wing configuration.....	32
Figure 22. Grid levels for the FE simulations of the full model configuration.....	33
Figure 23. Total drag coefficient of airfoil for different turbulence model (M=1.19)35	
Figure 24. Static pressure contours for Mach 1.19 (2D-Airfoil conf.).....	38
Figure 25. Static pressure contours for Mach 2 (2D-Airfoil conf.).....	39
Figure 26. Static pressure contours for Mach 2.5 (2D-Airfoil conf.).....	39
Figure 27. Static temperature contours for Mach 1.19 (2D-Airfoil conf.).....	40

Figure 28. Static temperature contours for Mach 2 (2D-Airfoil conf.).....	40
Figure 29. Static temperature contours for Mach 2.5 (2D-Airfoil conf.).....	41
Figure 30. Mach number contours for Mach 1.19 (2D-Airfoil conf.).....	41
Figure 31. Mach number contours for Mach 2 (2D-Airfoil conf.).....	42
Figure 32. Mach number contours for Mach 2.5 (2D-Airfoil conf.).....	42
Figure 33. Static pressure distribution over the airfoil surface	43
Figure 34. Heat transfer coefficient distribution over the airfoil surface.....	43
Figure 35. Static temperature distribution over the airfoil surface	43
Figure 36. Drag coefficients for different Mach numbers	44
Figure 37. Pressure coefficients for different Mach numbers.....	44
Figure 38. Flow domain used for the simulations of the 3D NACA 65-009 wing....	45
Figure 39. Static pressure contours for Mach 1.19 (3D-Clean wing conf.).....	46
Figure 40. Static pressure contours for Mach 2 (3D-Clean wing conf.).....	46
Figure 41. Static pressure contours for Mach 2.5 (3D-Clean wing conf.).....	46
Figure 42. Static temperature contours for Mach 1.19 (3D-Clean wing conf.)	47
Figure 43. Static temperature contours for Mach 2 (3D-Clean wing conf.)	47
Figure 44. Static temperature contours for Mach 2.5 (3D-Clean wing conf.)	47
Figure 45. Mach number contours for Mach 1.19 (3D-Clean wing conf.)	48
Figure 46. Mach number contours for Mach 2 (3D-Clean wing conf.).....	48
Figure 47. Mach number contours for Mach 2.5 (3D-Clean wing conf.)	48
Figure 48. Drag coefficients for different free stream velocities (3D-Clean wing conf.)	49
Figure 49. C_p distribution at 33% wing span (3D-Clean wing conf.).....	50
Figure 50. C_p distribution at 67% wing span(3D-Clean wing conf.).....	50
Figure 51. Variation of the maximum temperature and pressure on the wing surface	51
Figure 52. The FE model used to obtain the structural deformation	51
Figure 53. External loads applied on the FE model	52
Figure 54. Deformation contours on wing body for Mach 2.5 (mm)	53
Figure 55. Deformed and undeformed wing CFD model for Mach 2.5	54

Figure 56. C_P distribution for undeformed wing at 33% and 67% span	55
Figure 57. Static pressure contours of undeformed and deformed wings ($M=2.5$) ...	55
Figure 58. Static temperature contours of undeformed and deformed wings($M=2.5$)	56
Figure 59. Mach number contours of undeformed and deformed wings($M=2.5$).....	56
Figure 60. Flow domain for the missile equipped with NACA65-009 wing.....	57
Figure 61. Static pressure contours for Mach 1.19 (3D-Full model conf.).....	57
Figure 62. Static pressure contours for Mach 2 (3D-Full model conf.).....	58
Figure 63. Static pressure contours for Mach 2.5 (3D-Full model conf.).....	58
Figure 64. Static temperature contours for Mach 1.19 (3D-Full model conf.)	58
Figure 65. Static temperature contours for Mach 2 (3D-Full model conf.)	59
Figure 66. Static temperature contours for Mach 2.5 (3D-Full model conf.)	59
Figure 67. Mach number contours for Mach 1.19 (3D-Full model conf.).....	59
Figure 68. Mach number contours for Mach 2 (3D-Full model conf.).....	60
Figure 69. Mach number contours for Mach 2.5 (3D-Full model conf.).....	60
Figure 70. Drag coefficients for different free stream velocities (3D-Missile&Wing Conf.).....	61
Figure 71. C_P distribution at 33% wing span (3D-Missile&Wing Conf.).....	61
Figure 72. C_P distribution at 67% wing span (3D-Missile&Wing Conf.).....	62
Figure 73. Variation of maximum temperature and pressure on the wing surface	62
Figure 74. Finite element model of the missile with NACA wing	63
Figure 75. External loads applied on the FE model of the missile with NACA wing	63
Figure 76. Deformations of deformed body at free stream Mach number of 2.5	64
Figure 77. Static pressure contours of undeformed and deformed wings ($M=2.5$) ...	65
Figure 78. Static temperature contours of undeformed and deformed wings ($M=2.5$)	66
Figure 79. Mach number contours of undeformed and deformed wings ($M=2.5$).....	66
Figure 80. C_P distribution for undeformed wing at 33% and 67% span	67
Figure 81. The percent change in elastic properties of Aluminum 2000 series.....	75
Figure 82. Test setup	76

Figure 83. Test sample	76
Figure 84. Stress-strain relation for 25°C	77
Figure 85. Stress-strain relation for 200°C	77
Figure 86. Stress-strain relation for 250°C	78
Figure 87. Stress-strain relation for 300°C	78
Figure 88. The change in the yield and the tensile strength with temperature.....	79
Figure 89. The percent reduction of elastic modulus with exposed temperature.....	80

NOMENCLATURE

CFD	Computational fluid dynamics
FEM	Finite element methods
FSI	Fluid solid interaction
NACA	National Advisory Committee for Aeronautics
OES	Organized eddy simulation
RANS	Reynolds Averaged Navier-Stokes
SST	Shear stress transport
2D	Two-dimensional
3D	Three-dimensional
P	Pressure
P_{op}	Operating pressure
P_g	Gauge pressure
P_f	Face pressure
P_c	Cell pressure at neighboring exit face
P_e	Exit pressure
τ	Shear stress
F_R	Resultant aerodynamic force
F_D	Drag force
F_L	Lift force
F_N	Normal force
F_A	Axial force
F_d	Drag force per unit span
F_l	Lift force per unit span
α	Angle of attack
C_D	Wing drag coefficient
C_L	Wing lift coefficient
C_P	Wing pressure coefficient
U_∞	Free stream velocity
U_{n i,∞}	Velocity magnitude normal to the boundary(symmetry plane/wall)
R_{i,∞}	Riemann invariants
u	Velocity vector
a	Speed of sound
ρ	Density
S	Wing planform area
c	Chord length

μ	Absolute viscosity of air
k	Thermal conductivity of air
\dot{q}_w	Aerodynamic heating
h_w	Heat transfer coefficient at the wall
i	Internal energy
Φ	Dissipation term
ε	Normal strain
γ	Shear strain
σ	Normal stress
ν	Poisson ratio
b	Body force
μ_t	Eddy turbulence viscosity
S_{ij}	Turbulence stress
δ_{ij}	Kronecker delta
A_f	Cell face area
T_f	Film temperature
T_w	Wall temperature
γ_t	The ratio of specific heats
Ψ	Quantity term

CHAPTER 1

INTRODUCTION

In today's world, rockets and missiles are widely used in defense industry of many countries. Development of technology reveals the need of flight stabilization and hitting a target accurately. Control structures as wings are integrated to missiles in order to control the flow around the body. Missiles could be grouped in different ways according to their intended use. Table 1 shows the classification of missiles according to launching and target areas.

Table 1. Classification of missiles

Index	Launching	Target
AA	Air	Air
AS	Air	Surface
AU	Air	Underwater
SA	Surface	Air
SS	Surface	Surface
UU	Underwater	Underwater

Missiles moving through the air are subjected to a resistance during the flight. Some pressure and heat transfer effects are generated on them. These loads are investigated by a branch of an applied science called aerodynamics.

Increasing in the flow speed from subsonic to supersonic may bring some aerodynamic problems like capability of structural strength and aerodynamic heating. Designers are forced to get solution of these problems and to find better aerodynamic design. Wings are the most affected parts on the missile. Thus, they must be investigated more precisely. Wings are categorized into three main groups by their locations on missile body: canards, wings (or fins) and tail fins. As Figure 1 demonstrates, wings are located near the center of gravity while canards are placed in the missile nose and tail fins are assembled at the end of the missile body.

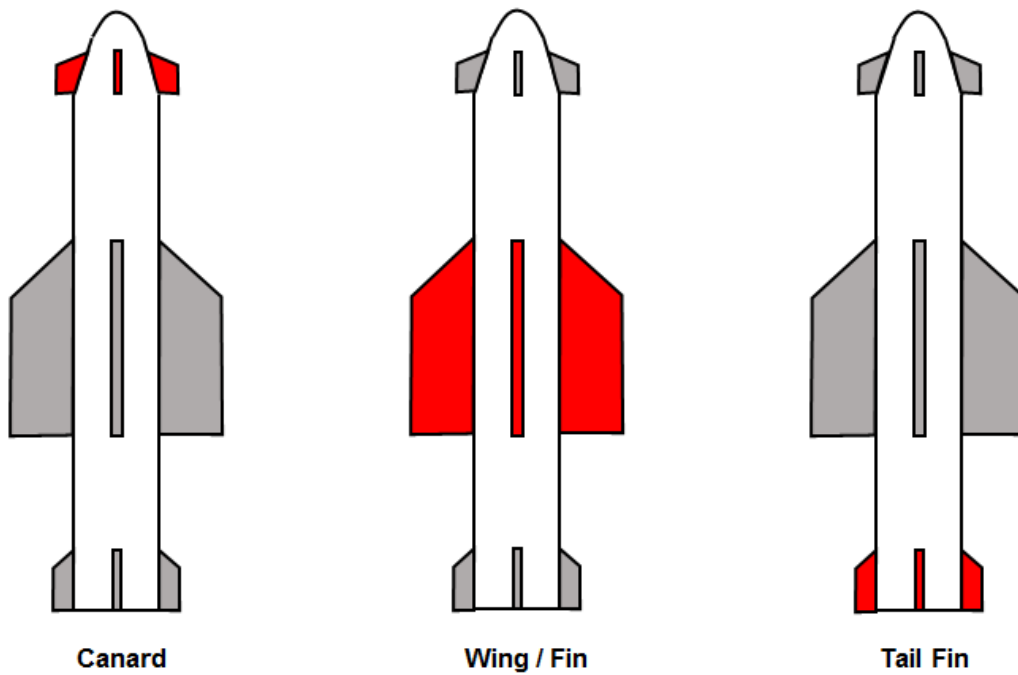


Figure 1. Canards, wings and tail fins

Wings showed in Figure 1 could be designed in both stationary and movable. Canards and fins are rarely used while the tail fins are highly preferred in missile technology. The main advantage of the canard is better maneuverability at low angles of attack. On the other hand using a canard on missile body causes a destabilizing effect and it requires large tail fins in order to keep the missile stable.

Wings or fins are the earliest form of the control surface of missiles. The usage of wings brings some advantages. The missile motion is not affected too much by the deflection of wings, so it allows the missile to be stabilized.

The tail fin is the most commonly used technology in missile systems. The missile using tail fins has the excellent maneuverability at high angles of attack. Therefore, many of the air defense systems and long range ballistic missiles have been used the tail fin.

The wing body is a region that is the most affected location on the missile from the nose to the end. Therefore, the effect on the missile aerodynamic performance is considerably higher. The evaluation of the missile aerodynamic performance is

defined by the drag and the lift coefficients. The detailed information about these parameters is given in Chapter 2. The change of the performance parameters could be obtained by investigating the drag and lift coefficients of wing during the flight. Thus, wings must be modelled or tested precisely under the flight conditions.

Aerodynamic design of wings is associated with the order of loads. Wings could be deformed due to these loads subjected to during flight. The wing deformation does not have to be very large shape changes. The deformation of a few millimeters in size affects adversely the formation of boundary layer and as a result of that the aerodynamic effects on wings changes. To obtain the wing deformation, the flow properties around the wing and the external loads on wing surfaces must be calculated. Firstly the flow characteristics must be classified then the flow properties are obtained from the solution of the conservation equations derived from some fundamental laws of physics.

Loads generated during the flight are obtained from the solution of the conservation equations given in Chapter 2. These calculations are nonlinear in body geometry, material property and boundary conditions. So, they could be solved numerically with CFD software. In addition to the flow condition, such as flight speed, altitude, etc., the aerodynamic loads are also related to the body deformation. The deformation and the aerodynamic loads are all interconnected because the exposed surface of the deformed body is different to the exposed surface of the undeformed body and different surface are generated different aerodynamic loads.

1.1. Deformation Phenomena

Many designers want to create a vehicle resistant to aerodynamic loads at supersonic speeds while it provides the desired aerodynamic performance. Aerodynamic loads are divided into two main group; aerodynamic pressure and aerodynamic heating. These loads are obtained from the solution of another nonlinear problem like the flow problem and must be solved precisely. In order to obtain the effect of deformation instantaneously, calculations are repeated for each step. The finite element method is the most known method for the solution of this type of problem.

Aerodynamic pressure is dominant for a flight at low speed while aerodynamic heating and its effects are more important than forces and moments for the flight at high speeds, such as supersonic and hypersonic.

The determination of instantaneous deformation of bodies and revising the change of flow conditions due to the deformation are quite complicated problems and they could be solved with a series of coupled CFD and FE calculations. There are two main methods of calculation;

- **One-Way FSI Coupling:** It includes the deformation calculations by using the aerodynamic loads in a sequence of CFD-FE simulation. It applies on the steady and the quasi-steady problems. The effect of deformation on the flow is not investigated in this method.
- **Two-Way FSI Coupling:** It includes the calculation of the deformations from the aerodynamic loads in a loop of CFD-FE simulation. After obtaining the deformed body, the flow conditions are revised with the deformed body and the simulations are repeated. The process of this method could be done automatically as well as manually. There are many commercial software solve the coupled problem automatically.

1.2. Literature Survey

Starting from 1940s, the effect of aerodynamic loads on structures, such as wings, fins, bodies etc., is the research field in lots of numerical and experimental studies.

In the prior works, the analytical studies were correlated to the test data and the test based design came to the forefront. By developing the numerical studies, more realistic results according to the test results were obtained.

One of the former studies about this research area was carried by Ericsson et al. (1978) that dealt with various wing configurations at supersonic and hypersonic speeds. The aerothermoelastic behavior of the missile fin at the range of $\alpha=0^\circ$ and $\alpha=10^\circ$ were aimed to be investigated. The effect of the missile nose bluntness and the nonlinear interactions of different parts were also investigated. According to the result, it was obtained that the aeroelastic characteristic is reduced by the thermodynamic effect. The interaction region between the missile body and the fin

structure had a negative effect on the aerodynamic characteristics of missile fins because the three-dimensional flow separation was occurred in the boundary layer on that location.

Another analytical design study by Sakata et al. (1975) carried out for an arrow wing and fuselage structure flying at Mach 2.7. The interaction among thermal stress, aeroelasticity and flutter characteristics was investigated. Two-dimensional and three-dimensional structural models were constructed to obtain loads and aeroelastic effects. The design study showed that the fuselage design is influenced by the high temperature environment, so modelling the fuselage has an important role on the aeroelastic effect.

Aerodynamic characteristics and efficiencies of delta and arrow wings were compared in the study of Wright et al. (1978). The aim of this comparison was to investigate the effect on the missile range. According to the result of this study, it was obtained that arrow wings are the most suitable wing type for the supersonic cruise missile and the lift-drag ratio of the arrow wing is higher than the delta wing. Also, the airfoil effectiveness at lower speed was improved by a reduction in wing sweep at the trailing edge section.

Johansen (1997) and Michael (1958) investigated airfoils at transonic flow regimes. The simplified form of e^n transition technique was adapted to a Navier-Stokes solver in order to predict the transition around various airfoils. The transition point was compared to the data obtained from the empirical correlations and experiments. The calculations showed the importance of the transition prediction for aerodynamic coefficients.

In another numerical study, Sani et al. (2014) simulated the rarefied flow field around a NACA0012 airfoil using the Navier-Stokes and direct simulation Monte Carlo methods for three different Knudsen numbers. The effect of Knudsen number on the leading edge shock, the lift to drag ratio (C_L/C_D) and velocity distribution over the NACA0012 airfoil were investigated. According to the result, the pressure coefficient and the density field agreed with the experimental data. It was obtained that an increase of Knudsen number causes an increase in the pressure coefficient at

the lower surface of the airfoil and the drag and the lift coefficients are approximately constant. The maximum ratio of aerodynamic coefficients occurred at $\alpha=25^\circ$.

Three-dimensional NACA0012 fin under unsteady flow condition were simulated by Hoffman et al. (2016). The simulation method in this study was an adaptive finite element method called General Galerkin method. Aerodynamic loads obtained from the flow simulation were compared with the flight test data. The comparison demonstrated that the similar result with the flight test data obtained from the simulations using General Galerkin method.

Giles et al. (2008) dealt with the enhancement of aerodynamic performances of an airfoil by using supersonic channel design. Numerical simulations were carried out to obtain the aerodynamic performance of the NACA66-206 airfoil. The flow was simulated in two- and three-dimensional at the free stream velocity range between Mach 2.5 and Mach 3. It was obtained that the drag forces on the airfoil are reduced, but the viscous loads are increased due to the increase over the fluid-solid interaction surfaces. The lift forces of the supersonic channel airfoil were obtained to be decreased with reference to the classical airfoil because of the reduction of the lifting surfaces.

The effects of thermal loading on the aeroelastic characteristics of a NASP like vertical fin were studied by Rodgers (1992). The result of the aerothermoelastic simulations were compared to the supersonic wind tunnel test data. The reduction in the stiffness of wing material at high temperatures caused a reduction in aeroelastic characteristics. Thus, model frequencies were decreased.

Space shuttle wings under the thermal-structural loadings were investigated in the study of Tamma et al. (1984). The finite element method was used to the exposed temperature field obtained from the steady-state heat transfer problem. Various wing configurations were investigated. It was demonstrated that the finite element approach could be applied to the shuttle wings subjected to aerodynamic loadings. This technique was considered as an efficient method for the thermomechanical analysis of insulated wing structures.

Aerothermoelastic wings stability was discussed in the study of Polli et al. (2008). The effect of the heat loads subjected to a sweep wing on the aerothermoelastic response was aimed to be investigated. The analytical model was developed and the exact solution was obtained. The results were conformed to the literature. It was obtained that the aeroelastic characteristics are influenced by the heat load and the heat induced the temperature distribution on the fin body.

In the study of Martinat et al. (2008), two- and three-dimensional simulations were conducted to obtain the aerodynamic characteristics of NACA0012. The Reynolds numbers in the simulations changed between 10^5 and 10^6 . The classical and the advanced RANS methods were compared to investigate the effect of the turbulence modelling performance. Comparisons made among the $k-\omega$ SST, the $k-\varepsilon$ Chien and the $k-\varepsilon$ OES turbulence models. The results showed that the $k-\omega$ SST model gives the most accurate result with a good prediction of aerodynamic coefficients during the motion. This study also showed that the two-dimensional studies are useful for the pre-design phase of the simulations and they could capture the structural dynamics in a good agreement with the three-dimensional simulations.

In the past recent years, flow around airfoils and wing structures were simulated numerically to obtain flow properties by Kurtulus et al. (2005; 2015; 2016). The aeroelastic behavior of airfoils at supersonic speeds was investigated in studies of Kayabasi et al. (2012) and Ozkokdemir et al. (2016; 2017).

One of the experimental studies about this research area was performed by Sheldahl et al. (1981) from the Sandia National Laboratory. 152 mm and 381 mm chord NACA0012 airfoils were investigated experimentally and the drag and the lift coefficients at Reynolds numbers range from 10^4 to 10^7 and at $\alpha=0^\circ$ to $\alpha=180^\circ$ were measured.

In the study of Borovoy et al. (1993), the effect of heat transfer of various wing tip configurations on the flow characteristic were investigated experimentally. Configurations of various fins assembled to the wing tip were the main discussion in this study. The wind tunnel tests were conducted under the flow condition of Mach 5 and Mach 8 and the order of Reynolds number was 10^6 . The test results showed that

the flow separation on the interaction line between fin and wing initiates at $\alpha=5^\circ$ and it causes an increase of the heat and the pressure on the fin surface. Outside of the interaction line, the bow and the normal shock waves were interacted with each other. Therefore, refracted shock waves were formed. These refracted waves caused an increase in heat transfer at the fin surface.

In the study of Alexander (1947), aerodynamic characteristics of a circular arc wing and a NACA65-009 wing structure were investigated experimentally. The flight tests were performed with the missile model equipped with these wings for the Mach number range from 0.85 to 1.22. The flight velocity was measured by the radar located at the ground. The drag force and the drag coefficient were calculated from the values of temperature and static pressure obtained from the radiosonde observations. The results showed that the drag coefficient of the NACA65-009 wing is lower than that produced by the circular-arc wing and the difference in the aerodynamic performance of two wings has maximum value near Mach 1. The results of the study of Alexander (1947) for the flow simulation of Mach 1.19 are used for the validation case of this thesis study. In another study of Alexander (1947), in order to investigate the effect of the aspect ratio and the sweep angle of these wing configurations were tested under the same flight conditions.

1.3. Motivation

The aim of this study is to investigate the effect of deformation on the aerodynamic performance of a missile fin operates at supersonic speeds. In order to obtain this effect, a methodology based on a series of CFD and FE simulations is used.

The methodology is applied to a NACA65-009 fin of missile model that is used in an experimental study conducted by Alexander (1947) from the Langley Research Center. This thesis study covers the numerical investigations that simulate the flight test conditions.

The short-term transient response of aeroelastic fins is investigated in some studies in the literature. To obtain long-term aero-elastic response of fins, it is seen that transient solution are not efficient. In this study, it is aimed to obtain a fast prediction of the solution with respect to other studies.

The objective of the thesis study is to investigate the flexible missile fins at supersonic speeds on the topic that is about the effect of deformation on the aerodynamic fin performance.

In Chapter 2, information about the basic definition about the flow and the structural problem and the methodology used in the numerical simulations are summarized. Chapter 3 covers the grid refinement studies for the method validation. Additionally, the turbulence models are discussed and the proper turbulence model is selected. The results of CFD and FE simulations are demonstrated in Chapter 4. As a final section, Chapter 5 includes the discussions about the result obtained in Chapter 4.

CHAPTER 2

METHODOLOGY

Fin deformation is directly related to the external loads and its material properties. It is important that these two parameters be precisely defined. Aerodynamic loads over the fin surface are obtained from the solution of the conservation equations under its flight regime (flight speed, altitude etc.). In this study, they are obtained numerically from the governing equations by using commercially available software. After pressure and heat transfer parameters distribution over the body surface are calculated, they are used for determining the deformation in the finite element model. Ansys Fluent and Abaqus are used for calculation of the flow and the structural problem, respectively.

2.1. Basic Definitions

Aerodynamic loads on fins shown in Figure 2 are due to two basic sources; pressure, P , acting normal to the surface of a body and shear stress, τ , tangential to the surface. The fluid pressure is due to the movement of the fluid over the body acts normal to the fin surface. On the other hand, the shear stress acts tangential to the surface can result only from the viscosity.

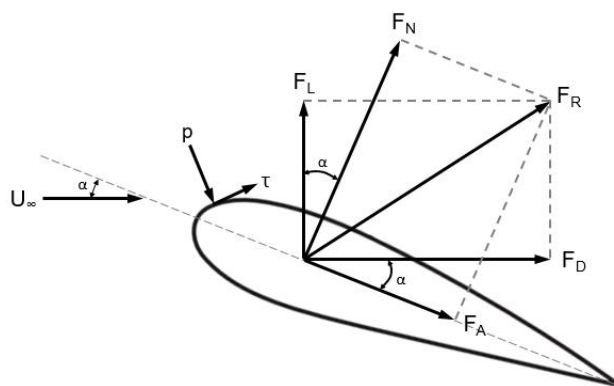


Figure 2. Resultant aerodynamic force and the components

The geometrical relation of these components is given in Equation (1) and Equation (2).

$$F_L = F_N \cos(\alpha) - F_A \sin(\alpha) \quad (1)$$

$$F_D = F_N \sin(\alpha) + F_A \cos(\alpha) \quad (2)$$

If the pressure and the shear stress integrate from the leading edge to the trailing edge on both upper and lower surface of fin, the aerodynamic moments could be obtained. The aerodynamic moment on a fin depends on the point about moments are taken. The drag (C_D) and the lift (C_L) coefficients are aerodynamic coefficients and they define the aerodynamic wing performance. For 3D simulations, these coefficients are given in Equation (3) and Equation (4).

$$C_D = \frac{F_D}{\frac{1}{2} \rho U_\infty^2 S} \quad (3)$$

$$C_L = \frac{F_L}{\frac{1}{2} \rho U_\infty^2 S} \quad (4)$$

For 2D simulations, the lift and drag coefficients are given by Equation (5) and Equation (6), respectively.

$$C_d = \frac{F_d}{\frac{1}{2} \rho U_\infty^2 c} \quad (5)$$

$$C_l = \frac{F_l}{\frac{1}{2} \rho U_\infty^2 c} \quad (6)$$

The compressive effects become dominant from the sonic speed to the supersonic speed. In supersonic regimes, there is a region formed near the body wall called the boundary layer. The flow speed decreases and becomes zero at the body wall due to the no slip condition on the wall. In the boundary layer, decreasing in the kinetic energy of the fluid causes an increase in heat energy and the temperature is driven by

the combined mechanism of the frictional dissipation and the thermal conduction. The velocity and the temperature profiles in this layer are given in Figure 3.

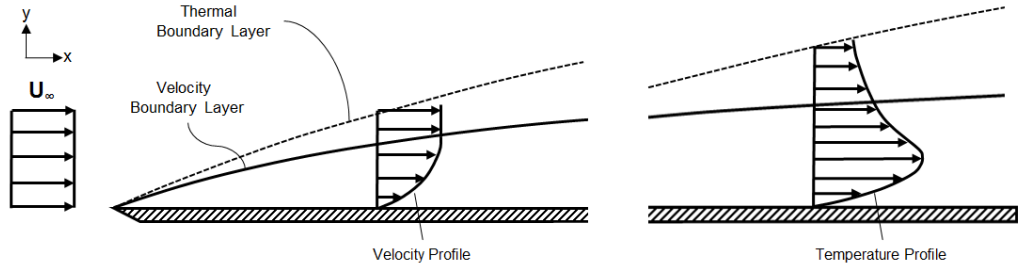


Figure 3. Velocity and temperature profile inside the boundary layer

The shear stress at the fin wall given in Equation (7) is dictated by the slope of velocity profile at the wall. The slope of temperature profile is also very important because it governs the aerodynamic heating at the fin wall given in Equation (8).

$$\tau_w = \mu \left(\frac{dV}{dy} \right)_{y=0} \quad (7)$$

$$\dot{q}_w = -k \left(\frac{dT}{dy} \right)_{y=0} \quad (8)$$

In order to obtain the motion of the fluid, the fluid domain induced an infinitesimal control volume given in Figure 4. Mass, momentum and energy balance equations for the suitable type of flow (unsteady, viscous, compressible etc.) are applied to the control volume then the solution for the control volume is applied whole fluid domain. These balance equations are also called the conservation equations.

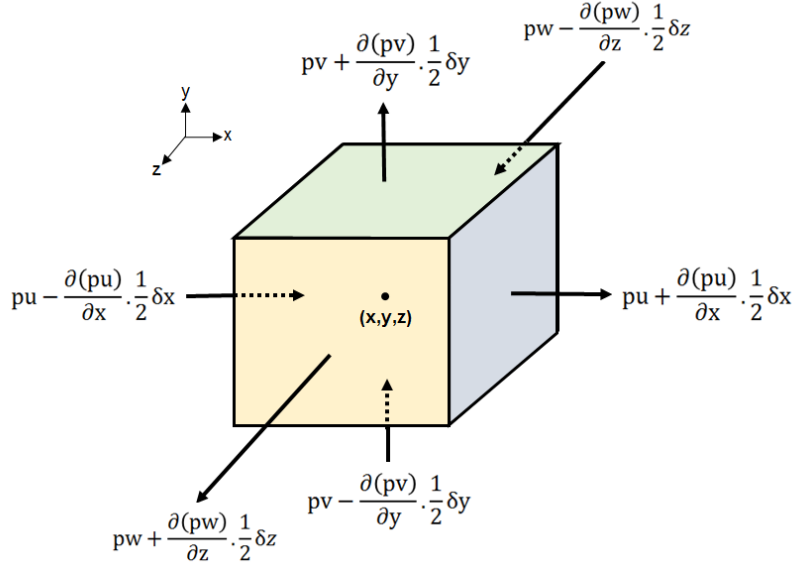


Figure 4. Control volume

The steady, viscous and three-dimensional conservation equations for the compressible fluid are given between Equation (9) and Equation (13).

$$\text{div}(\rho \mathbf{u}) = \mathbf{0} \quad (9)$$

$$\text{div}(\rho u \mathbf{u}) = -\frac{\partial p}{\partial x} + \text{div}(\mu \text{grad } u) \quad (10)$$

$$\text{div}(\rho v \mathbf{u}) = -\frac{\partial p}{\partial y} + \text{div}(\mu \text{grad } v) \quad (11)$$

$$\text{div}(\rho w \mathbf{u}) = -\frac{\partial p}{\partial z} + \text{div}(\mu \text{grad } w) \quad (12)$$

$$\text{div}(\rho i \mathbf{u}) = -p \text{div } \mathbf{u} + \text{div}(k \text{grad } T) + \Phi \quad (13)$$

The conservation equations represent the basic physical fundamentals that dictate the air flow characteristics. In this study they must be solved for the flow properties over fins under the supersonic flow condition. The solution of the conservation equations can be conducted in two different ways; analytical or numerical.

The governing equations of the flow problem are highly nonlinear, partial differential or integral equations. So there are no analytical solutions that solve these equations

exactly. The analytical approach simplifies the governing equations and the resulting simplified equations become linear and can be solved analytically. This approach provides simple tools for rapid and approximate calculations. It is generally used in the preliminary design phase.

The numerical solution is another general approach for solving the conservation equations. The integrals and partial derivatives in these equations are discretized to an algebraic form and they solved at discrete time points and positions. This process is the main subject of the computational fluid dynamics. In this thesis work, the well-known commercial computational fluid dynamic software, Ansys Fluent, is used for solving conservation equations by using the finite volume technique with the SIMPLE-type fully implicit algorithm.

The random behavior of the turbulent flow is obtained by solving the turbulence equations with various turbulence models, such as Spalart-Allmaras, k- ϵ , k- ω and Reynolds stress model. The detail information about these turbulence models could be found in Versteeg et al. (2007). In this thesis study, only k- ϵ and k- ω models are investigated. The turbulence kinetic energy (k), dissipation rate (ϵ) and turbulence frequency (ω) equations for these models are given between Equation (14) and Equation (17).

- k- ϵ turbulence model;

$$\frac{\partial(\rho k)}{\partial t} + \text{div}(\rho k \mathbf{U}) = \text{div}[\mu_k \text{grad}(k)] + 2\mu_t S_{ij} \cdot S_{ij} - \rho \epsilon \quad (14)$$

$$\frac{\partial(\rho \epsilon)}{\partial t} + \text{div}(\rho \epsilon \mathbf{U}) = \text{div}\left[\frac{\mu_t}{1.3} \text{grad}(\epsilon)\right] + 1.44 \frac{\epsilon}{k} 2\mu_t S_{ij} \cdot S_{ij} - 1.92 \rho \frac{\epsilon^2}{k} \quad (15)$$

- k- ω turbulence model;

$$\frac{\partial(\rho k)}{\partial t} + \text{div}(\rho k \mathbf{U}) = \text{div}\left[\left(\mu + \frac{\mu_t}{2}\right) \text{grad}(k)\right] + P_k - 0.09 \rho k \omega \quad (16)$$

where $P_k = \left(2\mu_t S_{ij} \cdot S_{ij} - \frac{2}{3} \rho k \frac{\partial U_i}{\partial x_j} \delta_{ij}\right)$

$$\frac{\partial(\rho\omega)}{\partial t} + \text{div}(\rho\omega\mathbf{U}) = \text{div} \left[\left(\mu + \frac{\mu_t}{2} \right) \text{grad}(\omega) \right] + P_\omega - 0.075\rho\omega^2 \quad (17)$$

where $P_\omega = 0.553 \left(2\rho S_{ij} \cdot S_{ij} - \frac{2}{3} \rho\omega \frac{\partial U_i}{\partial x_j} \delta_{ij} \right)$

After the flow properties such as pressure and heat transfer parameters over the structural body are calculated, the body must be investigated in detail by using the finite element technique. In this technique, whole body is modeled by the small pieces of structure called the finite element shown in Figure 5. The basic equations of solid mechanics are written for each piece of structure then they are solved numerically. The deformed body shape under the aerodynamic loads could be defined by three displacement components in three directions. Each of the displacement components is a function of coordinates. The strain generated in the body could be expressed in terms of the displacement components. The strain-displacement relations for three-dimensional problems are defined as in Equation (18).

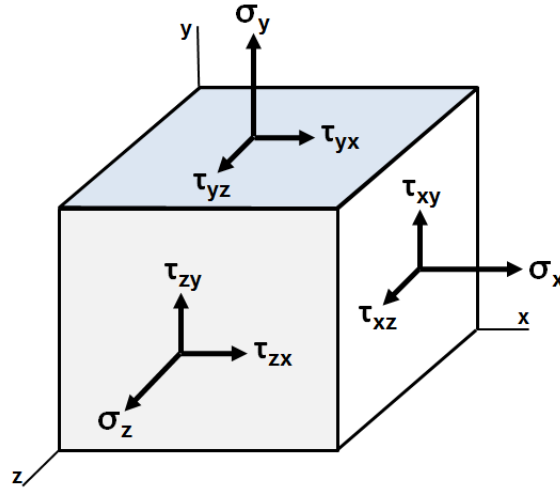


Figure 5. Stresses on a finite element

$$\begin{Bmatrix} \varepsilon_x \\ \varepsilon_y \\ \varepsilon_z \\ \gamma_{xy} \\ \gamma_{yz} \\ \gamma_{zx} \end{Bmatrix} = \begin{bmatrix} \frac{\partial}{\partial x} & 0 & 0 \\ 0 & \frac{\partial}{\partial y} & 0 \\ 0 & 0 & \frac{\partial}{\partial z} \\ \frac{\partial}{\partial y} & \frac{\partial}{\partial x} & 0 \\ 0 & \frac{\partial}{\partial z} & \frac{\partial}{\partial y} \\ \frac{\partial}{\partial z} & 0 & \frac{\partial}{\partial x} \end{bmatrix} \begin{Bmatrix} u \\ v \\ w \end{Bmatrix}, \quad \{\varepsilon\} = [d]\{\delta\} \quad (18)$$

For linear isotropic 3D solids, the stress-strain relations called Hooke's law are given in Equation (19).

$$\begin{Bmatrix} \sigma_x \\ \sigma_y \\ \sigma_z \\ \tau_{xy} \\ \tau_{yz} \\ \tau_{zx} \end{Bmatrix} = \frac{E}{(1+\nu)(1-2\nu)} \begin{bmatrix} 1-\nu & \nu & \nu & 0 & 0 & 0 \\ \nu & 1-\nu & \nu & 0 & 0 & 0 \\ \nu & \nu & 1-\nu & 0 & 0 & 0 \\ 0 & 0 & 0 & \frac{1}{2}(1-2\nu) & 0 & 0 \\ 0 & 0 & 0 & 0 & \frac{1}{2}(1-2\nu) & 0 \\ 0 & 0 & 0 & 0 & 0 & \frac{1}{2}(1-2\nu) \end{bmatrix} \begin{Bmatrix} \varepsilon_x \\ \varepsilon_y \\ \varepsilon_z \\ \gamma_{xy} \\ \gamma_{yz} \\ \gamma_{zx} \end{Bmatrix} \quad (19)$$

$$\{\sigma\} = [E]\{\varepsilon\}$$

According to the conservation of momentum, the body must be in equilibrium. The equilibrium means that the externally applied loads on the body and the internal stresses developed by the loads must be in balance. The equations of equilibrium are given in Equation (20).

$$\begin{bmatrix} \frac{\partial}{\partial x} & 0 & 0 & \frac{\partial}{\partial y} & 0 & \frac{\partial}{\partial z} \\ 0 & \frac{\partial}{\partial y} & 0 & \frac{\partial}{\partial x} & \frac{\partial}{\partial z} & 0 \\ 0 & 0 & \frac{\partial}{\partial z} & 0 & \frac{\partial}{\partial y} & \frac{\partial}{\partial x} \end{bmatrix} \begin{Bmatrix} \sigma_x \\ \sigma_y \\ \sigma_z \\ \tau_{xy} \\ \tau_{yz} \\ \tau_{zx} \end{Bmatrix} - \begin{Bmatrix} b_x \\ b_y \\ b_z \end{Bmatrix} = \begin{Bmatrix} 0 \\ 0 \\ 0 \end{Bmatrix}, \quad [d]^T\{\sigma\} - \{b\} = \{0\} \quad (20)$$

In order to obtain the solution of structural part, the number of governing equations and unknowns should be satisfied. It is seen between Equation (19) and Equation (21) that there are fifteen equations and fifteen unknowns ($u, v, w, \varepsilon_x, \varepsilon_y, \varepsilon_z, \gamma_{xy}, \gamma_{yz},$

γ_{zx} , σ_x , σ_y , σ_z , τ_{xy} , τ_{yz} and τ_{zx}), so the problem is solvable. The deformed shape of the body could be obtained from the displacements in the solution of these equations.

2.2. Procedure of the Method

In order to obtain the effect of deformation on the aerodynamic performance, the methodology given in Figure 6 is used. The methodology is based on a series of conjugate CFD simulations and thermo-mechanic FE simulations.

In the CFD simulations, Ansys Fluent that uses the fully implicit finite volume method is used to solve the conservation equations. On the other hand, Abaqus Standard is used for simulating the load cases to obtain the structural deformation by using the finite element technique.

The interaction between the CFD and the FE simulations are done manually. The aerodynamic loads are exported from the flow simulations and they are applied to the finite element model as boundary conditions. After solving the structural simulations, the deformation is obtained and flow simulations are repeated with the revised flow domain that includes the deformed body.

The procedure of the method includes four main steps;

- In the first step, the steady flow simulations are carried out for the certain flow condition (constant Mach number, altitude and α). The aerodynamic loads, such as pressure and thermal loads are calculated by using the finite volume technique. In the flow simulations, the grid is also generated inside the solid region for the conjugate solution. Thus, the transferred heat through the solid region could be calculated. By solving the flow problem, the aerodynamic forces are also calculated and these are used for obtaining the aerodynamic coefficients. In order to get correct solution of the flow problem, these coefficients must be compared to the experimental data conducted for the same flow conditions. The flow simulations in the first step are continued until the valid result is obtained. After obtaining the similar result with the experimental data, the aerodynamic loads generated on the wetted areas are transferred to the finite element model as a boundary condition.

- In the second step, the thermal loads, such as heat transfer coefficient and sink temperature distributions calculated at the wetted surfaces are applied to the thermal FE model to obtain the body temperatures. In the thermal FE simulations, all surfaces except the wetted surfaces are assumed to be adiabatic; so, no heat transfer calculation is made at these surfaces. Second step of the procedure could be skipped by using the body temperatures exported from the CFD simulations directly. Because of the huge mapping time and the possibility of making mistakes during mapping process, this option is not selected.
- In the third step, the grid generated for the thermal FE simulations are used by changing element type to the 3D stress element. The deformation is calculated by using the temperature distribution obtained from the second step in addition to the pressure distribution obtained from the CFD simulations. In the structural FE model, the combined effect of the aerodynamic pressure and the thermal stress due to the temperature distribution over the body on the deformation is obtained.
- In the fourth and last step, the flow domain is revised with the deformed body obtained from the previous step. The boundary layer is recreated in accordance with the deformed body while exterior dimensions of the flow domain remain the same. The change in the aerodynamic coefficients for the deformed and the undeformed body shows the effect of deformation on the aerodynamic performance.

The detailed information about elements and fluid properties in the simulations is given in the following chapters.

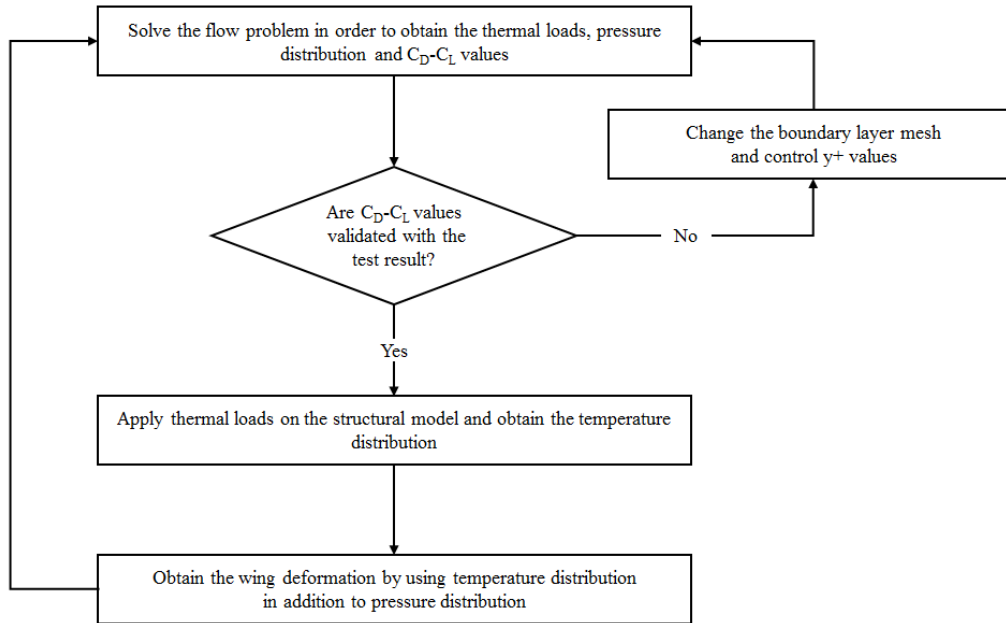


Figure 6. Procedure of the method

CHAPTER 4

VALIDATION STUDIES

The validation case study for the grid refinement and the turbulence model selection are discussed in this chapter.

3.1. Simulation Models

A symmetrical wing based on 245mm chord with NACA65-009 airfoil is selected as a validation case. Coordinates of the NACA65-009 airfoil surface are obtained from Abbott (1945) and the chapter is shown in Figure 7.

The aerodynamic coefficients obtained from the flight test conducted by Alexander (1947) are compared with the flow simulations in this thesis study. In the experimental study of Alexander (1947), a missile model equipped with a NACA65-009 fin/wing is tested at the supersonic speed from Mach 0.85 to Mach 1.22. Inside of the missile model; there is no frame and plate to enhance the stiffness of the system. Thus, the missile body is modelled as a hollow cylinder in the simulations. The altitude and Reynolds level at the flight test is not stated in the test report. Therefore, the flow properties are taken at the sea level conditions for all flow simulations. Figure 8 demonstrates the flight test model.

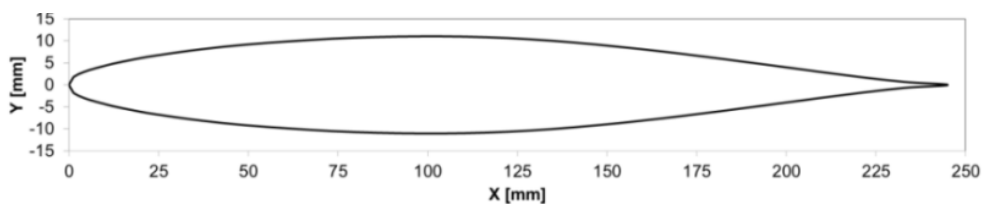


Figure 7. NACA 65-009 airfoil

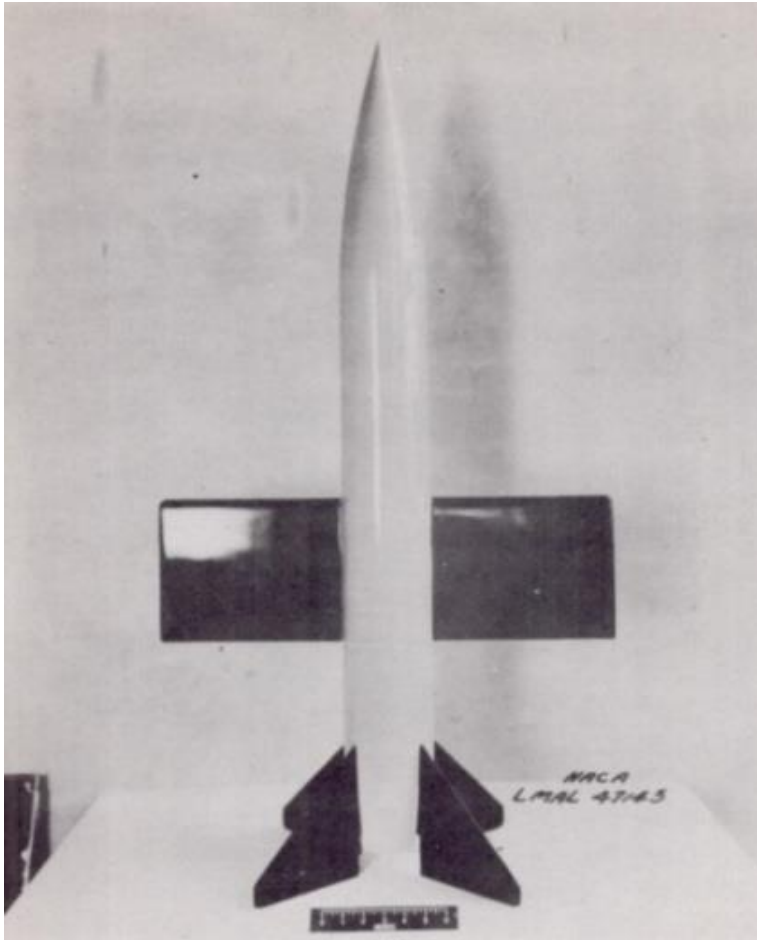


Figure 8. Flight test model by the Langley Laboratory, by Alexander (1947)

Two- and three-dimensional numerical simulations are categorized into three main groups in which the two-dimensional simulations are carried out in order to validate the method and three-dimensional simulations are carried out for investigating the effect of deformation

1. NACA airfoil configuration (2D)
2. NACA clean wing configuration (3D)
3. Missile body equipped with NACA wing configuration (3D)

3.1.1. CFD Simulation Models

The two- and three-dimensional flow domains given in Figure 9 and Figure 10 are used for the CFD simulations. It is shown in these figures that the inlet section of the domain is defined as the pressure far field boundary condition and the pressure outlet is used at the outlet region. The exterior surface of the airfoil and the fin is defined as the two-sided wall boundary conditions.

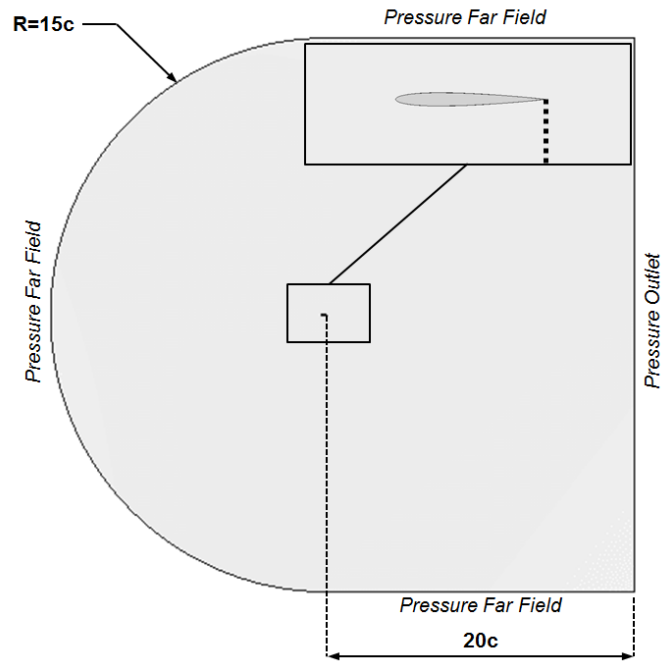


Figure 9. Two-dimensional flow domain and boundary conditions

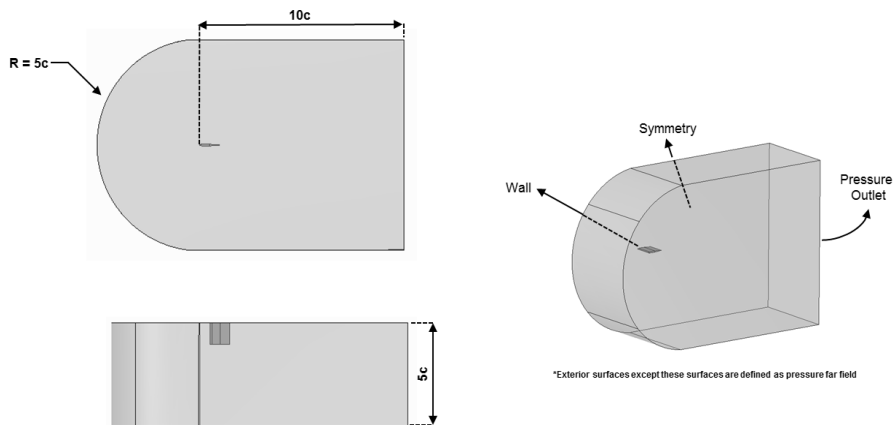


Figure 10. Three-dimensional flow domain and boundary conditions

The boundary conditions defined are summarized as follows;

- Pressure far field condition: The pressure far field boundary condition is a non-reflecting boundary condition based on the Riemann invariants given in Equation (21) and Equation (22). By using these invariants, the normal velocity and the sound speed applied on the boundary given in Equation (23) and Equation (24) could be calculated. Using these values velocity, temperature and pressure at the boundary face could be calculated.

$$R_{\infty} = U_{n,\infty} - \frac{2a_{\infty}}{\gamma_t - 1} \quad (21)$$

$$R_i = U_{n,i} - \frac{2a_i}{\gamma_t - 1} \quad (22)$$

$$U_n = \frac{1}{2}(R_i + R_{\infty}) \quad (23)$$

$$a = \frac{\gamma_t - 1}{4}(R_i - R_{\infty}) \quad (24)$$

- Pressure outlet condition: The boundary condition pressure is used as the static pressure of the fluid at the outlet plane and it is extrapolated all other conditions from the interior of the domain.

$$P_f = 0.5(P_c + P_e) + \left[P_e - \frac{\sum 0.5(P_c + P_e)A_f}{\sum A_f} \right] \quad (25)$$

- Symmetry condition: A zero flux of all quantities no convective flux across a symmetry boundary is assumed. Therefore, the normal velocity component at the symmetry plane is zero.

$$U_n = 0 \quad \text{at the symmetry boundary} \quad (26)$$

$$\frac{d\Psi}{dn} = 0 \quad \text{at the symmetry boundary} \quad (27)$$

- Two-sided wall condition: The wall zone is assumed to have a fluid or solid region on each side. The shear stress and the velocity magnitude at the wall is zero because of the no slip conditions. The law of the wall for temperature

derived from the analogy between the heat and the momentum transfer is used for calculating the heat transfer coefficient. The detail information about the analogy could be found in the documentation of Ansys Fluent r15.

$$\tau_w = 0 \text{ and } U = 0 \text{ at the wall} \quad (28)$$

$$\dot{q}_w = h_w(T_f - T_w) \quad (29)$$

In the flow simulations, the pressure-based segregated algorithm in which the pressure equation is derived from the continuity and the momentum equations and these equations are solved sequentially. The fluid is assumed to be the ideal gas, so the fluid density is calculated from the ideal gas law for compressible flows that is given in Equation 30. Another physical property of the fluid is the viscosity that is obtained from the kinetic theory by Sutherland (1893) and given in Equation 31.

$$\rho = \frac{P_{op} + P_g}{RT} \quad (30)$$

$$\mu = 1.716 \times 10^{-5} \left(\frac{T}{273.11} \right)^{\frac{3}{2}} \frac{383.67}{T + 110.56} \quad (31)$$

Isentropic relations in Anderson (2017) are used to calculate the total/static temperatures and pressures for a certain free stream velocity. The altitude of the flight test data was not available, so, the flow properties are taken at sea level conditions and $\alpha=0^\circ$. The transferred heat from the fluid region to the solid region is calculated by performing conjugate solution. Simulations have been stopped until all of the residuals have reached a value below 10^{-5} .

3.1.2. FE Simulation Models

The FE simulations are carried out only for the three-dimensional model because the deformation is investigated only for the three-dimensional simulations. The structural deformation is calculated by using FE models demonstrated in Figure 11 and Figure 12.

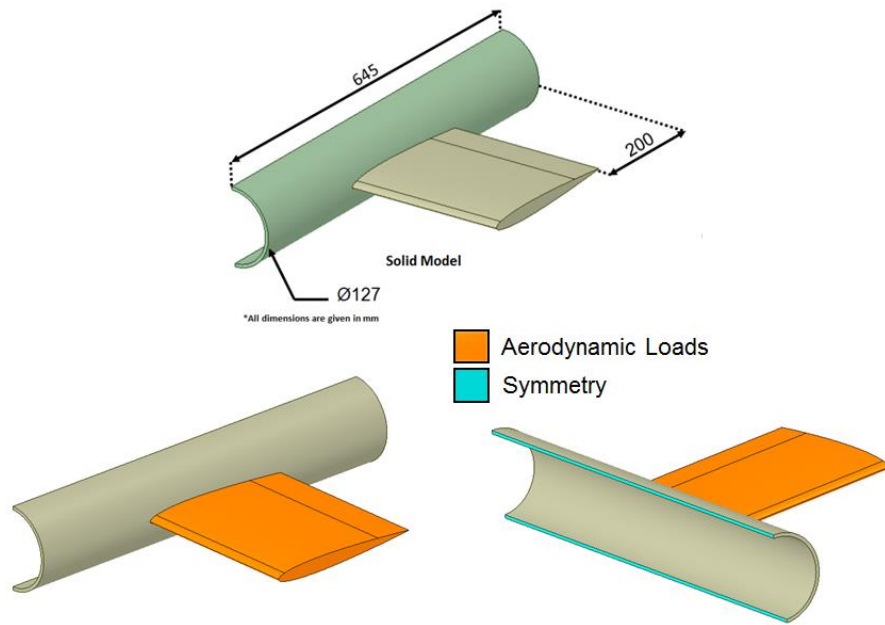


Figure 11. FE simulation of the clean wing configuration

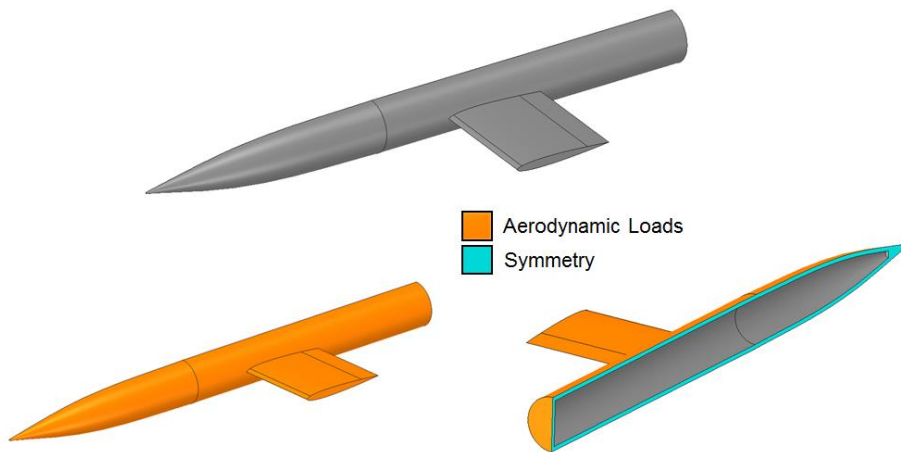


Figure 12. FE simulation of the full model configuration

As shown in Figure 11 and Figure 12, the FE model is constrained only in the symmetry plane. No translational and rotational motions are allowed in the normal direction to that plane. In order to simulate the flight condition, the fixed constraint boundary condition except the symmetry condition could not be modelled. The FE simulations are performed by the inertia relief technique that involves balancing externally applied forces on a free or partially constrained body with the loads

derived from constant rigid body acceleration. The inertia forces of the body are included in the structural simulation that balances the aerodynamic loading. The detail information about the inertia relief simulations could be found in the theory manual of the Abaqus r6.13 from DS Simulia (2013).

The FE model is a section of the flight test model in the study of Alexander (1947). The missile body and the wing are both deformable and made by aluminum 2000 series and the material properties are given in Table 2. The reduction on the elasticity of aluminum material is modelled in the FE simulations to get correct deformations. In order to obtain the percent reduction of the elasticity of the aluminum 2000 series, the material characterization tests are performed at the Atılım University Metal Forming Center of Excellence. The detailed information about these tests is given in Appendix A.

Table 2. Mechanical and thermal properties of aluminum 2000 series

Property	Value
Density (kg/m ³)	2770
Young Modulus (MPa)	72814*
Poisson Ratio	0.33
Expansion (1/°C)	2.2x10 ⁻⁵
Conductivity (W/m.K)	120
Specific Heat (J/kg.K)	900

* Nominal value; it is defined by changing with the temperature

3.2. Grid Refinement Study

In this section, the detail of the grid refinement studies of the CFD and the FE simulations are discussed separately.

3.2.1. Grid Refinement for the CFD Simulations

For the grid refinement study for the CFD simulations, the two- and three-dimensional flow domain given in Figure 9 and Figure 10 are used. In the three-dimensional flow domain, the grid generated inside the boundary layer is composed of the structured elements and the unstructured elements are generated outside of the boundary layer. For the two-dimensional flow simulations, the quadrilateral grid

structure is used in every section in the domain. The grid element types used in the CFD simulations are shown in Figure 13.

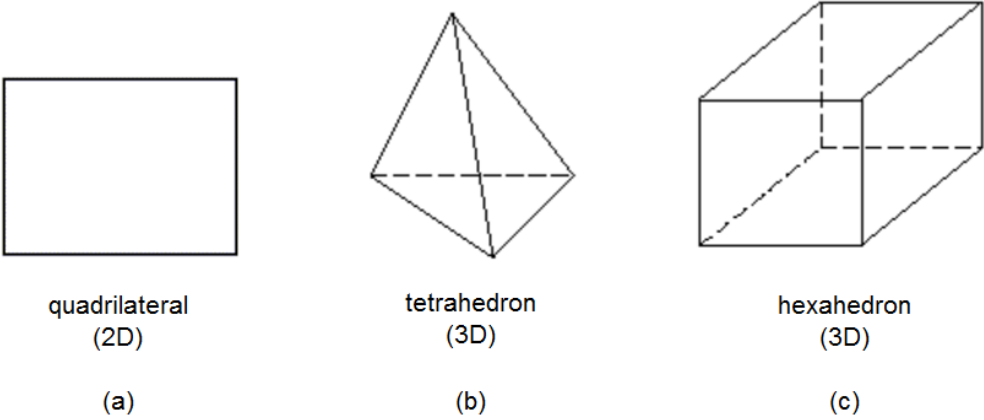


Figure 13. Element types used in the CFD simulations

The grid is also generated inside of the airfoil for the two-dimensional simulations and fin body for the three-dimensional simulations to perform the conjugate solution. The y^+ values inside the boundary layer are about 1 for all meshes for two- and three-dimensional flow simulations. The grid generated for all mesh levels are shown in Figure 14 and Figure 15. The numbers of elements generated for the grid refinement study are presented in Table 3

Table 3. Grid refinement study for the CFD simulations

Mesh Level	# of Elements
Coarse mesh (2D)	746 936
Medium mesh (2D)	1 685 730
Fine mesh (2D)	2 326 766
Wing Coarse Mesh (3D)	7 475 146
Wing Medium Mesh (3D)	11 197 318
Wing Fine Mesh (3D)	15 586 768

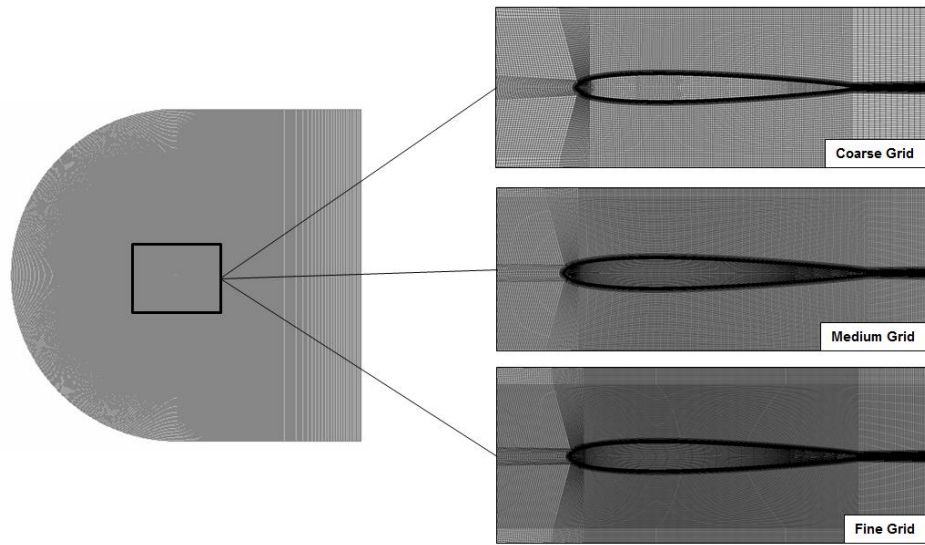


Figure 14. Grid levels for the 2D flow simulations

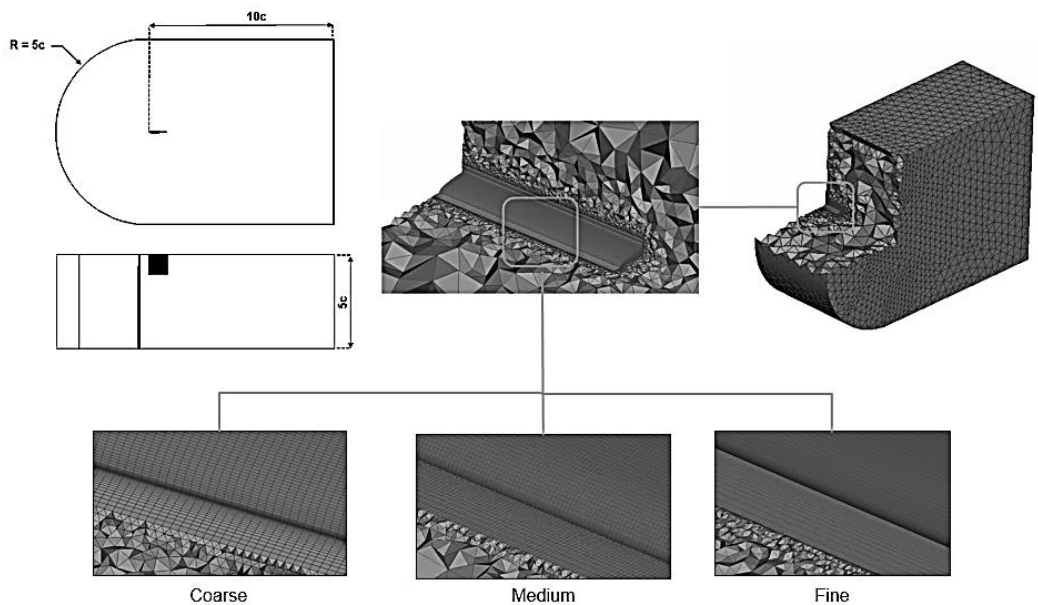


Figure 15. Grid levels for 3D flow simulations

In order to make comparisons with the flight test data, the two- and three-dimensional grid refinement studies are performed only for $M=1.19$. The comparison of the total drag coefficients for different grid levels is shown in Figure 16 and Figure 18, respectively. The total drag coefficient is the summation of the pressure drag and the viscous drag coefficients shown in Figure 17 and Figure 19. The results showed that the solutions for medium and fine meshes of two- and three-dimensional

simulations are very close to each other. So, all of the simulations are performed with medium meshes.

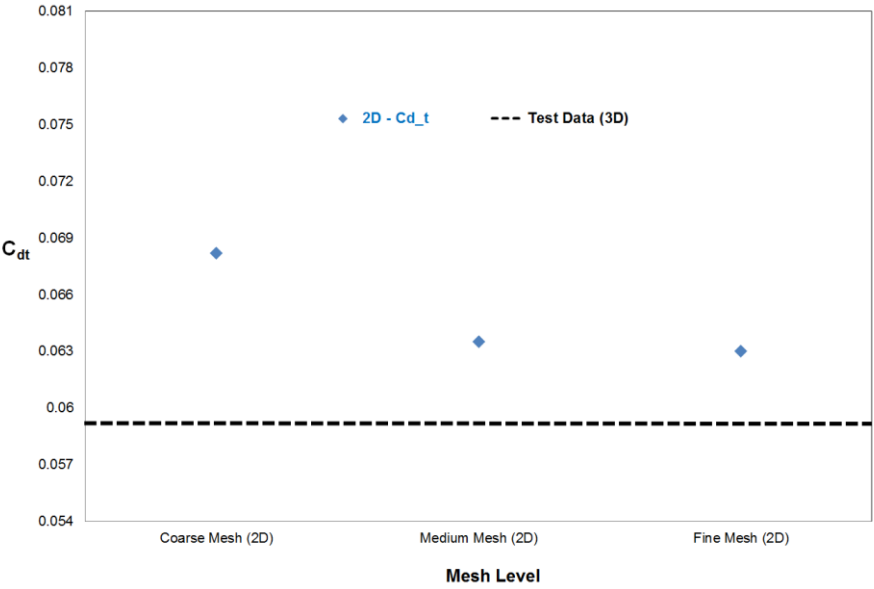


Figure 16. Total drag coefficient of airfoil for different meshes

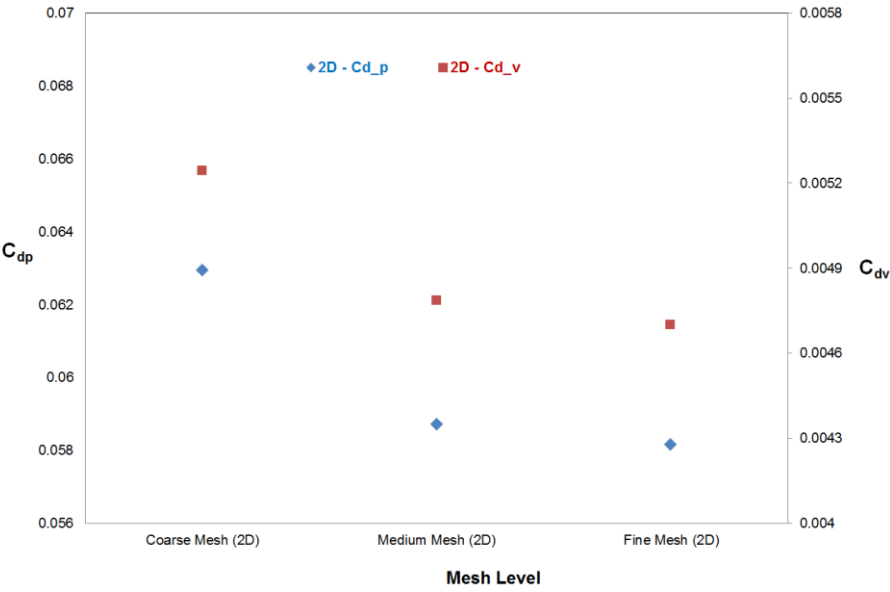


Figure 17. Pressure and viscous drag coefficient of airfoil for different meshes

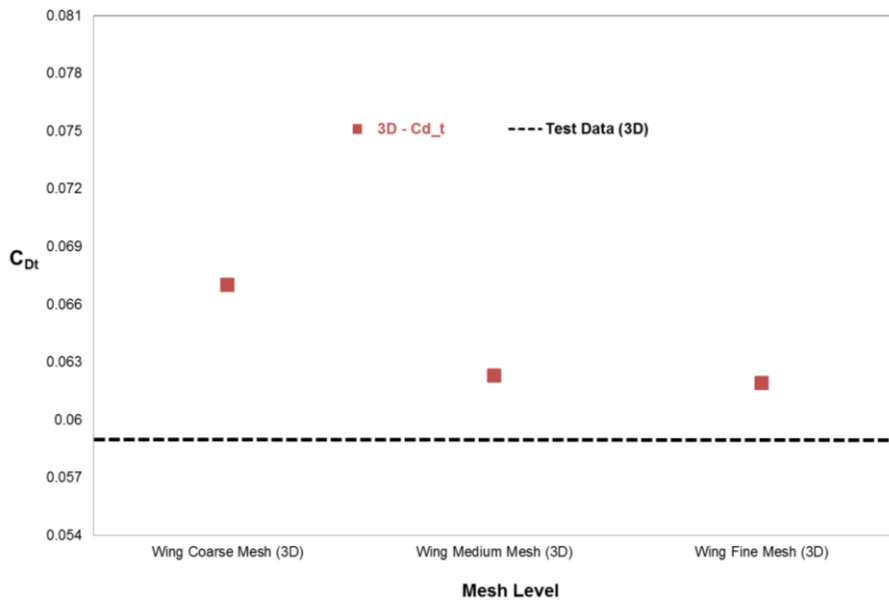


Figure 18. Total drag coefficient of wing for different meshes

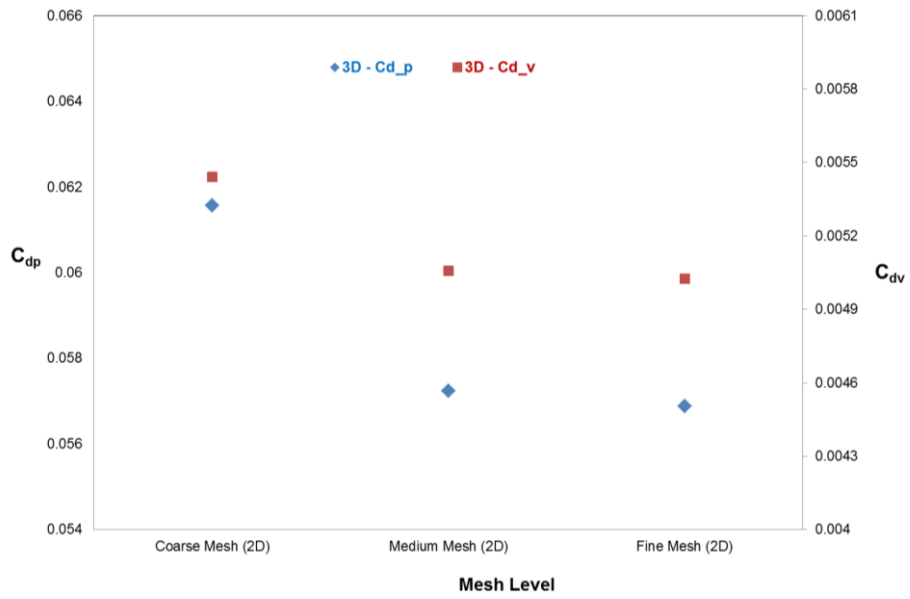


Figure 19. Pressure and viscous drag coefficient of wing for different meshes

3.2.2. Grid Refinement for the FE Simulations

The grid refinement study of FE simulations are carried out with the three-dimensional models shown in Figure 11 and Figure 12. In the FE grids generated, both 8-node hexahedral and 4-node tetrahedral stress elements given in Figure 20 are used to construct the structural models.

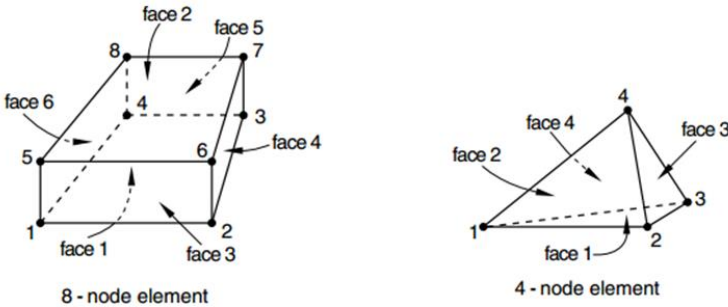


Figure 20. 3D stress elements for FE simulations

To obtain the correct grid level for the FE simulations, three different grids shown in Figure 21 and Figure 22 are generated. Table 4 demonstrates the number of elements for the corresponding grid level.

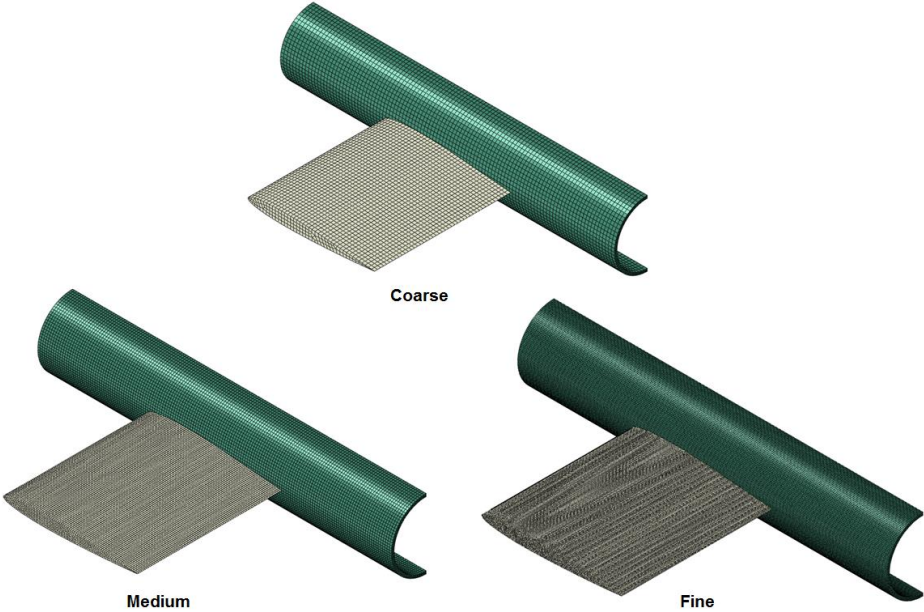


Figure 21. Grid levels for the FE simulations of the clean wing configuration

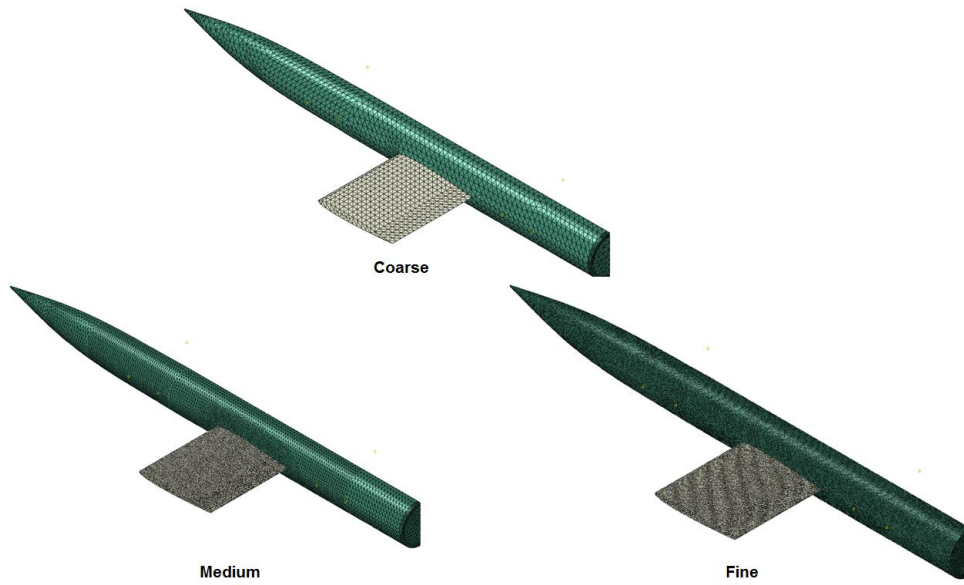


Figure 22. Grid levels for the FE simulations of the full model configuration

Table 4. Grid refinement study for the FE simulations

Mesh Level	# of Elements
Coarse mesh (Case-1)	30496
Medium mesh (Case-1)	73032
Fine mesh (Case-1)	234232
Coarse mesh (Case-2)	284789
Medium mesh (Case-2)	692039
Fine mesh (Case-2)	1743938

The sufficiency of the refinement of FE grid is controlled by making comparison of the resultant forces in the FE model with those in the CFD model. Table 5 shows the resultant force comparisons of CFD and FE simulations. According to Table 5, the resultant forces obtained for the fine and the medium grid levels are very similar. Therefore, the remaining study is carried out with the medium grid.

Table 5. Grid refinement study for FE simulations

Conf.	Mesh Level	CFD Resultant Force (N)	FE Resultant Force (N)	Difference %
Clean Wing	Coarse mesh	1038.4	963.7	7.2
Clean Wing	Medium mesh	965.6	933.7	3.3
Clean Wing	Fine mesh	959.4	935.4	2.5
Full Model	Coarse Mesh	1023.7	959.2	6.3
Full Model	Medium Mesh	951.8	929.0	2.4
Full Model	Fine Mesh	945.7	925.9	2.1

3.3. Turbulence Models

The effect of the turbulence model on the flow characteristics is simulated in four different turbulence models; Standard/Realizable k- ϵ model and Standard/SST k- ω model. In this section, the flow simulations are solved only for the two-dimensional airfoil at Mach 1.19 and $\alpha=0^\circ$. It is assumed that the results are applicable for the three-dimensional simulations. Each of the models is used in the same flow condition and the detail of the boundary conditions are given in Chapter 3.1.

The effect of the turbulence method on the aerodynamic performance or the total drag coefficient is given in Figure 23. According to the Figure 23, the result for SST k- ω turbulence model is more suitable result for the flight test data.

Turbulence models are also investigated in many numerical studies in literature. In the study of Martinat et al. (2008), comparisons made between k- ω SST, k- ϵ Chien and k- ϵ OES turbulence model to investigate the effect of turbulence modelling performance. It was obtained that k- ω SST model gives the most accurate results with a good prediction of the aerodynamic coefficients during the motion. D. C. Eleni et al. (2012) investigated the behavior of the airfoil at different conditions and to establish a verified solution method in their study. It was obtained that the most accurate model is k- ω SST model, second come the Spalart - Allmaras and latest in precision is the Realizable k- ϵ .

In the PhD thesis of Lillard (2011), the turbulence modelling for the shock wave and the turbulent boundary layer interactions is investigated. According to the results, it

is stated that the Spalart – Allmaras and the k- ω SST models predict the pressure peak in the shock wave very well.

In the view of such information, the SST k- ω turbulence model is used in the remaining study.

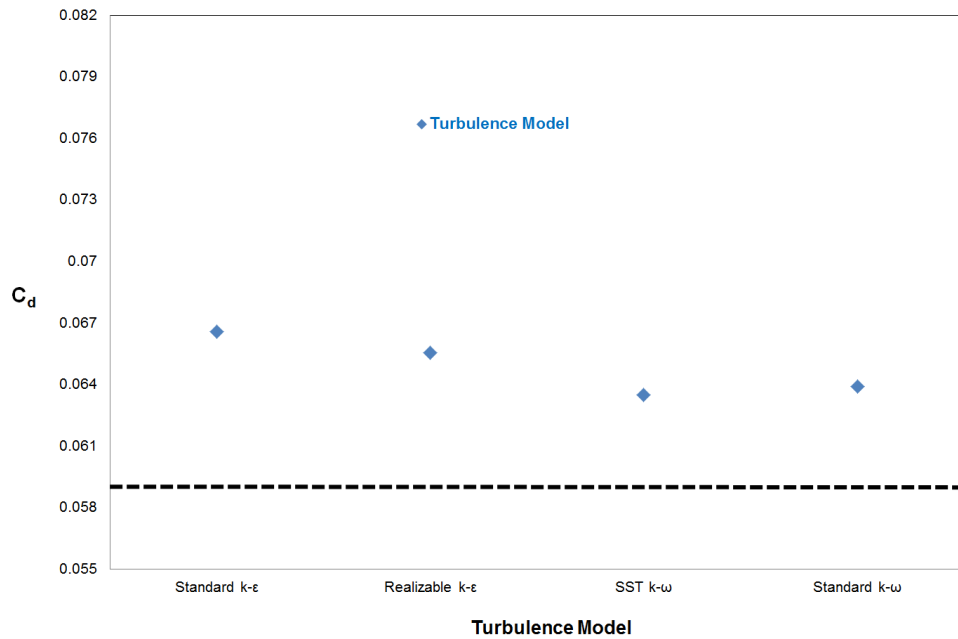


Figure 23. Total drag coefficient of airfoil for different turbulence model (M=1.19)

CHAPTER 5

RESULTS OF THE NUMERICAL SIMULATIONS

In this chapter, the results of two and three-dimensional simulations are presented. The 2D simulations are carried out for the method validation in order to investigate how the flow properties, such as heat loads and pressure, are affected by the change of the free stream velocity. Thus, the deformation is not calculated in the 2D simulations. The effect of the fin deformation is taken into account in the flow problem in the 3D simulations that are divided into two main groups. In the first group, the flow over a 3D NACA 65-009 wing body is modelled. The effect of the missile body is included in the flow simulations in the second group of the 3D simulations.

4.1. Simulations for the 2D NACA 65-009 Airfoil

In the two-dimensional simulations of NACA 65-009 airfoil, the solution method defined is aimed to be validated. The quasi-steady simulations are carried out for the Mach number of 1.19, 2 and 2.5 at $\alpha=0^\circ$ and Reynolds number of 10^6 . The 2D medium level mesh given in Figure 14 is used in the 2D flow simulations.

The contours of the flow properties that are the static pressure, the static temperature and the velocity distribution over the flow domain are demonstrated between Figure 24 and Figure 32. Also the external loads (static pressure, static temperature and heat transfer coefficient) exerted on the wing surfaces are calculated from the leading edge to the trailing edge and they are demonstrated from Figure 33 to Figure 35.

It is seen that the static temperature and the static pressure decrease along the wing surface. Approximately 80% of the thermal loading acts on the wing surfaces are placed near leading edge. Therefore, it is expected that the temperature difference between the leading edge and the other sections on the airfoil is considerably high and this difference could cause the thermal stress that is investigated in the 3D simulations.

An increase in the flow speed at a point on airfoil surface causes an increase in the external loads calculated at the same point but the heat transfer coefficient has a random behavior near the leading and the trailing edge. The main reason of the oscillation on that location is due to the instability of the flow speed. Because of the relation between the heat transfer coefficient and the flow speed, the thermal loads oscillate at that location.

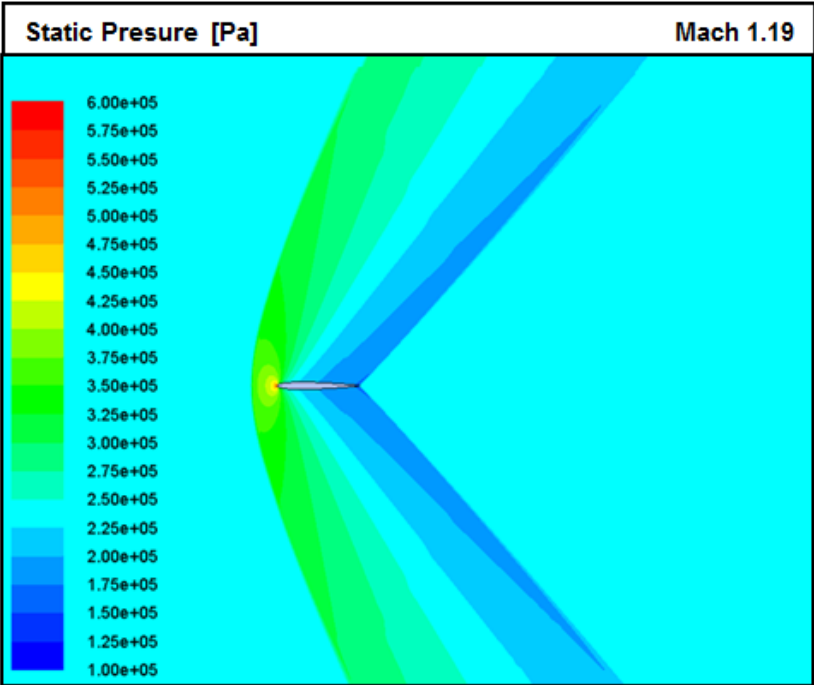


Figure 24. Static pressure contours for Mach 1.19 (2D-Airfoil conf.)

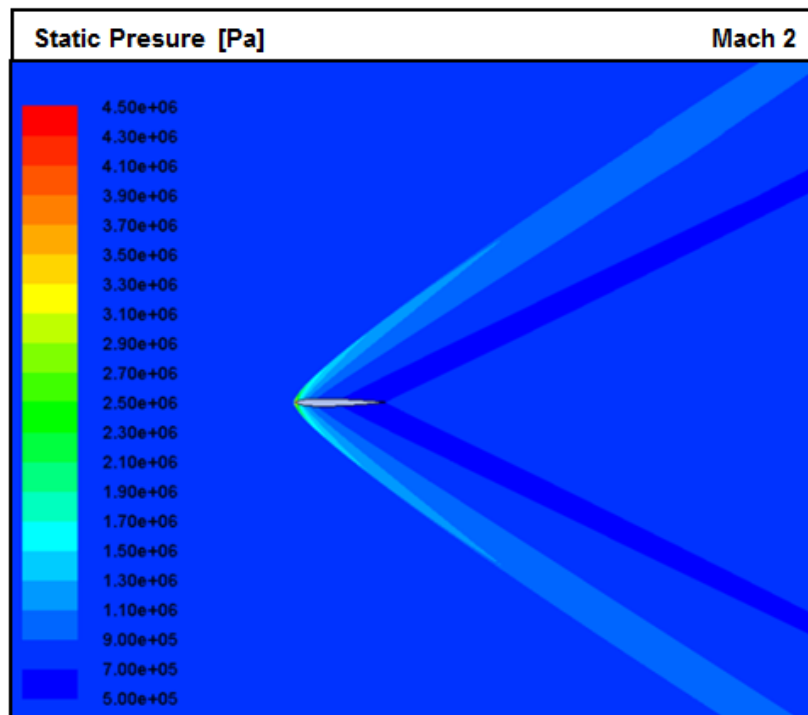


Figure 25. Static pressure contours for Mach 2 (2D-Airfoil conf.)

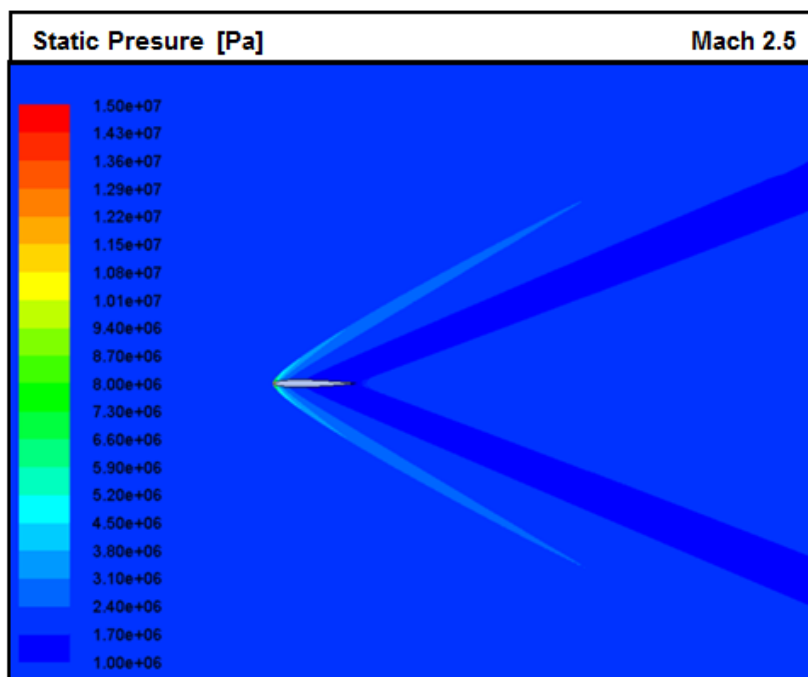


Figure 26. Static pressure contours for Mach 2.5 (2D-Airfoil conf.)

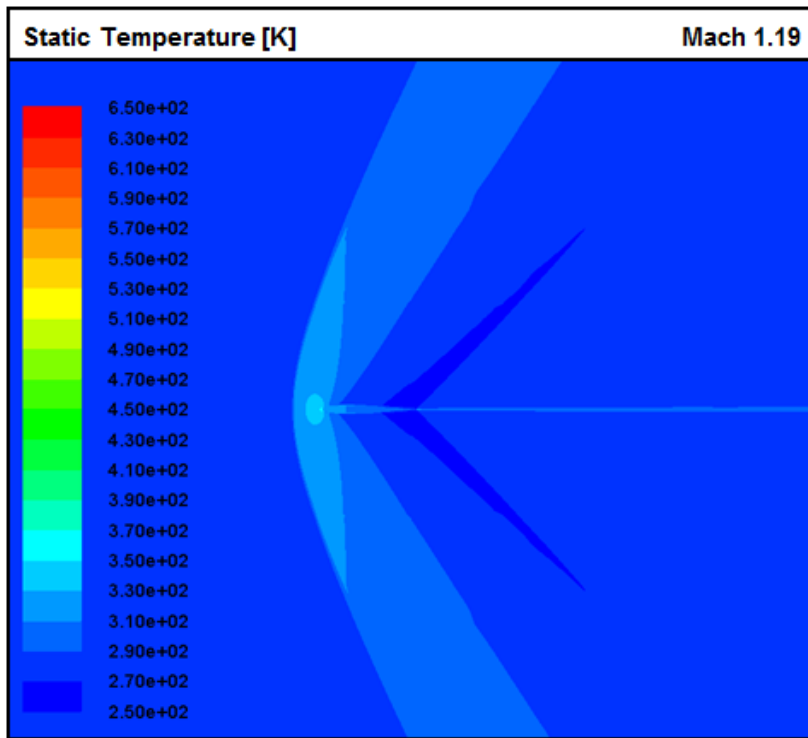


Figure 27. Static temperature contours for Mach 1.19 (2D-Airfoil conf.)

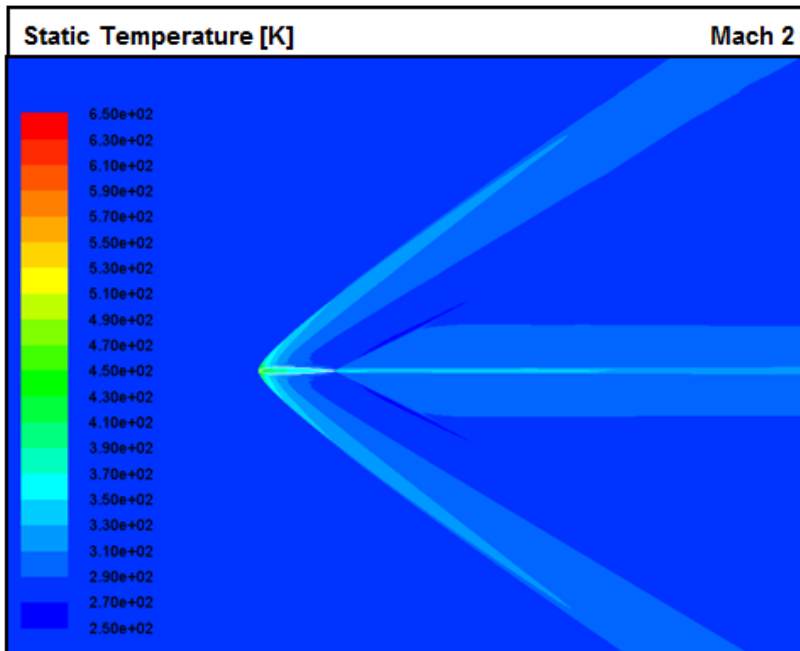


Figure 28. Static temperature contours for Mach 2 (2D-Airfoil conf.)

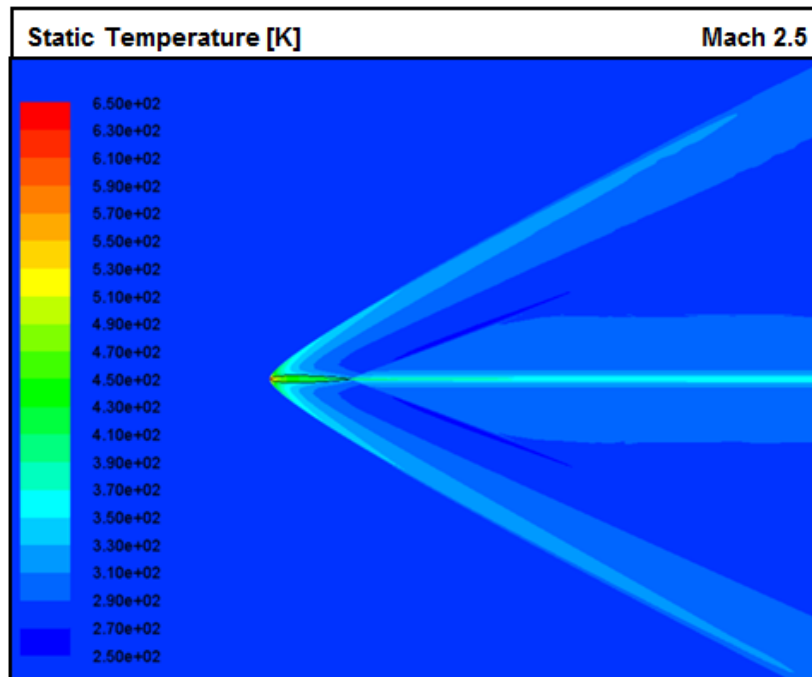


Figure 29. Static temperature contours for Mach 2.5 (2D-Airfoil conf.)

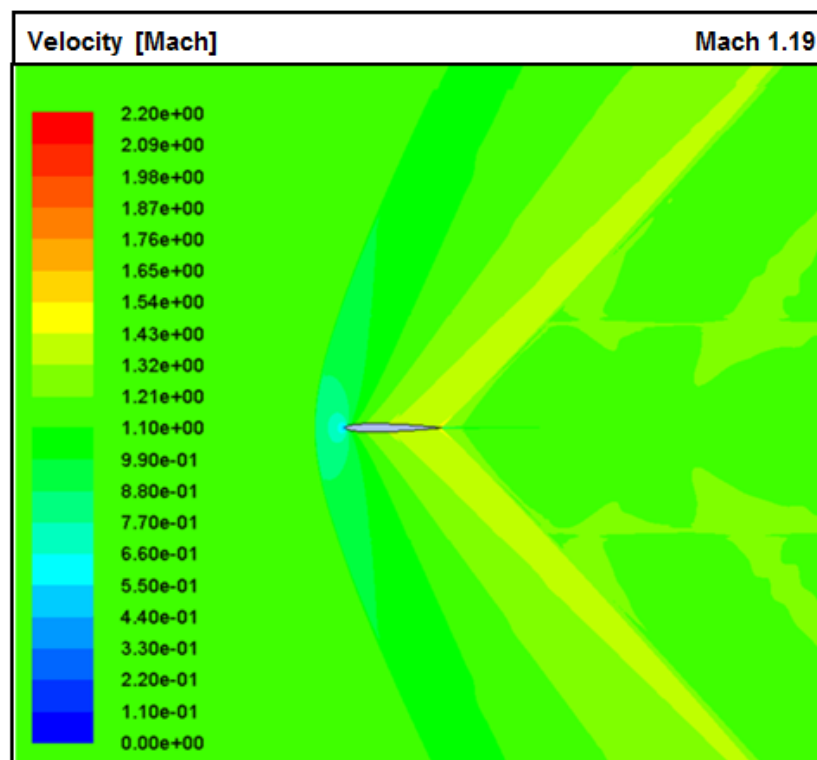


Figure 30. Mach number contours for Mach 1.19 (2D-Airfoil conf.)

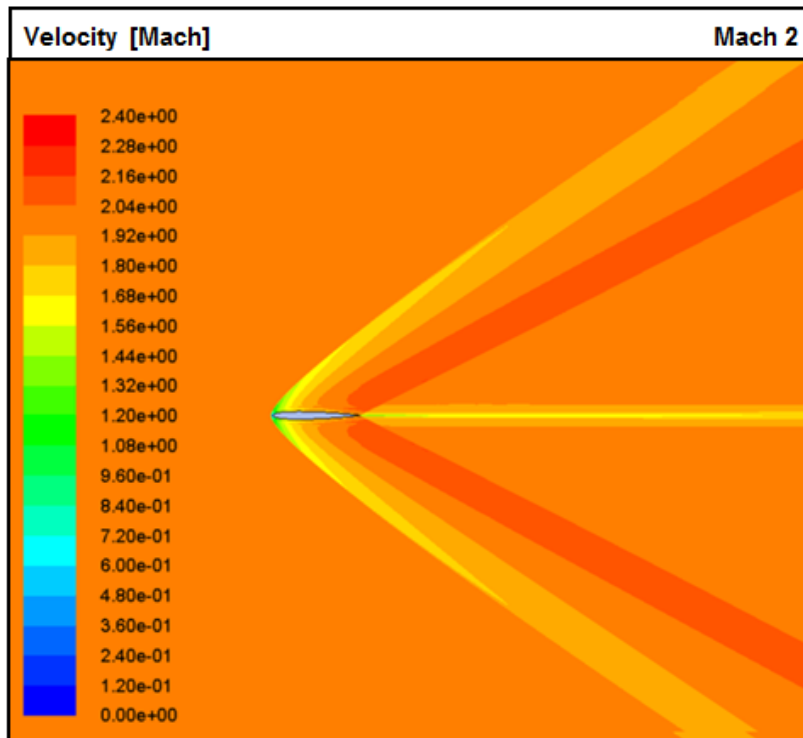


Figure 31. Mach number contours for Mach 2 (2D-Airfoil conf.)

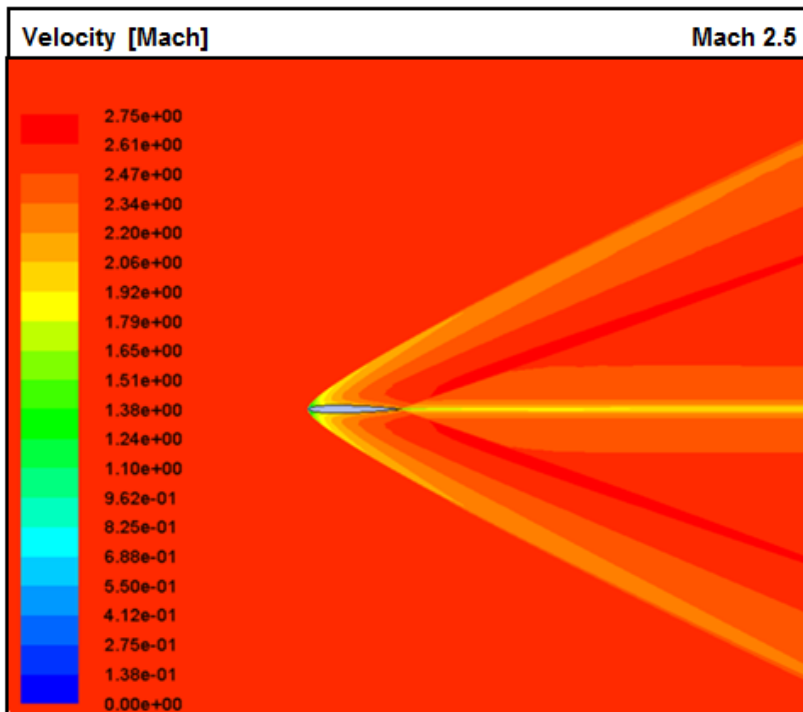


Figure 32. Mach number contours for Mach 2.5 (2D-Airfoil conf.)

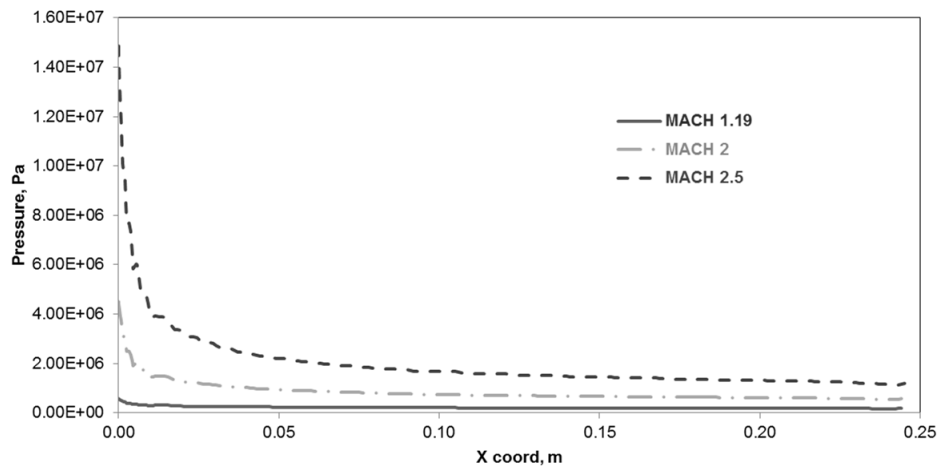


Figure 33. Static pressure distribution over the airfoil surface

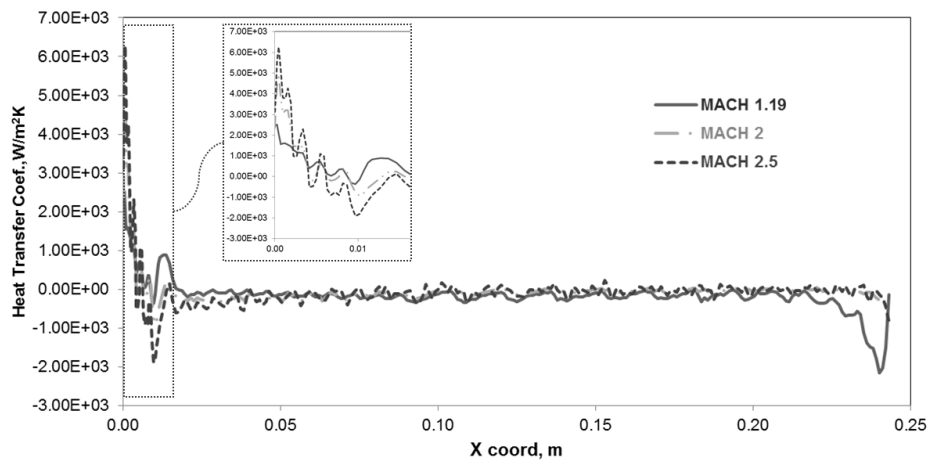


Figure 34. Heat transfer coefficient distribution over the airfoil surface

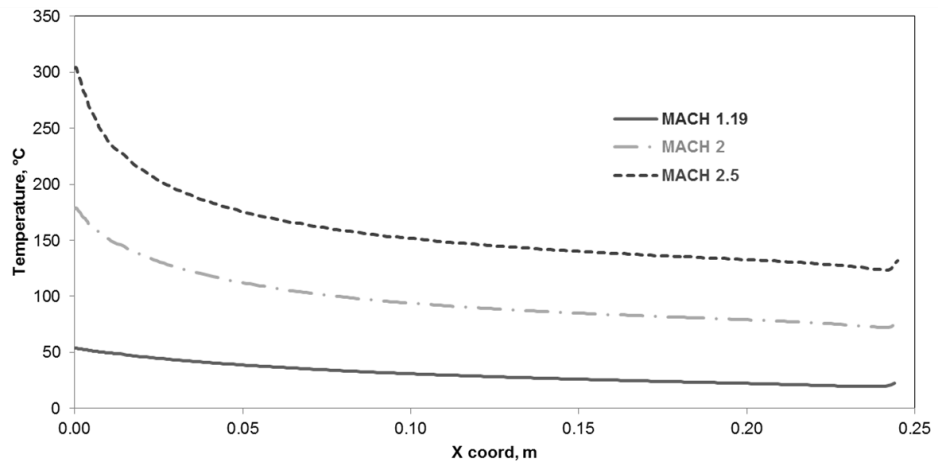


Figure 35. Static temperature distribution over the airfoil surface

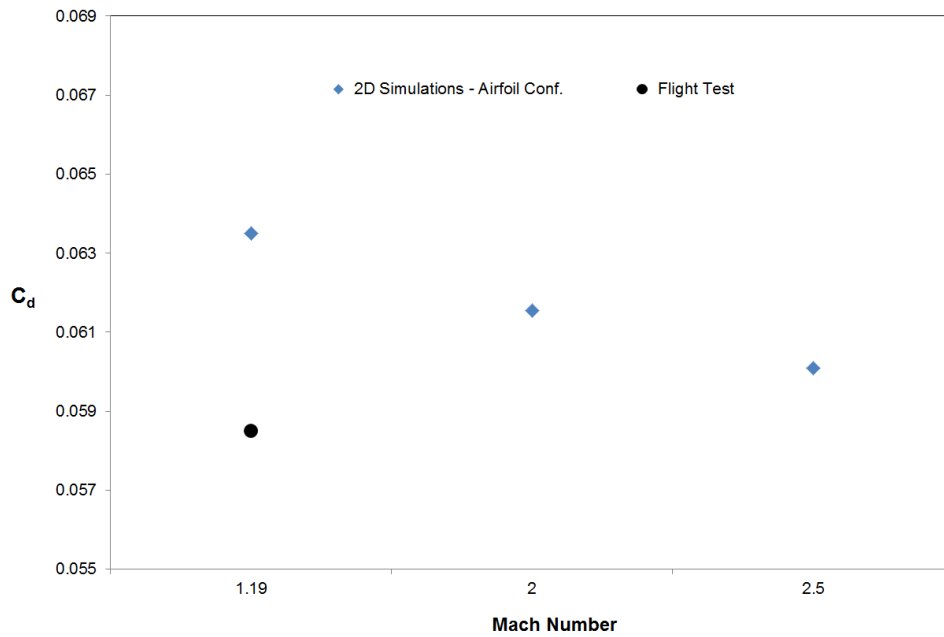


Figure 36. Drag coefficients for different Mach numbers

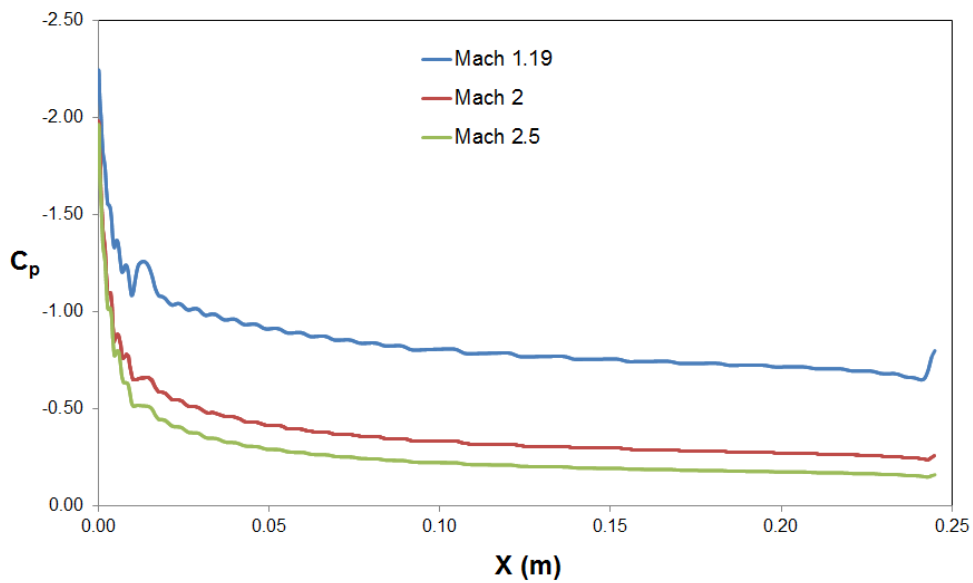


Figure 37. Pressure coefficients for different Mach numbers

The change of the drag coefficient and the pressure coefficient with the flow speed is presented in Figure 36 and Figure 37, respectively. The effect of the missile body and the three-dimensional flow effect at the wing tip and the wing root sections could not be modelled in the two-dimensional simulations. This is the main reason of the

difference that is about 8.5% in drag coefficients given in Figure 36 between the flight test and the two-dimensional flow simulations. According to Figure 37, the pressure coefficient distribution at upper and lower surface of the wing is almost the same for all free stream velocities. As a result of that, the lift coefficient of the wing becomes zero.

4.2. Simulations for the 3D NACA 65-009 Wing

In the two-dimensional simulation, the effect of the wing tip and the three-dimensional behavior of the fluid on the wing could not be simulated. Therefore, the three-dimensional simulations of the NACA 65-009 wing are carried out to solve the flow problem more realistic.

This section covers the numerical simulations that include flow simulations and FE simulations. In the first part three-dimensional NACA 65-009 wing simulations, the flow problem has been solved for three different Mach numbers at $\alpha=0^\circ$ and Reynolds number of 10^6 as given in Chapter 3.1. The flow domain used for the flow simulations in this section is shown in Figure 38.

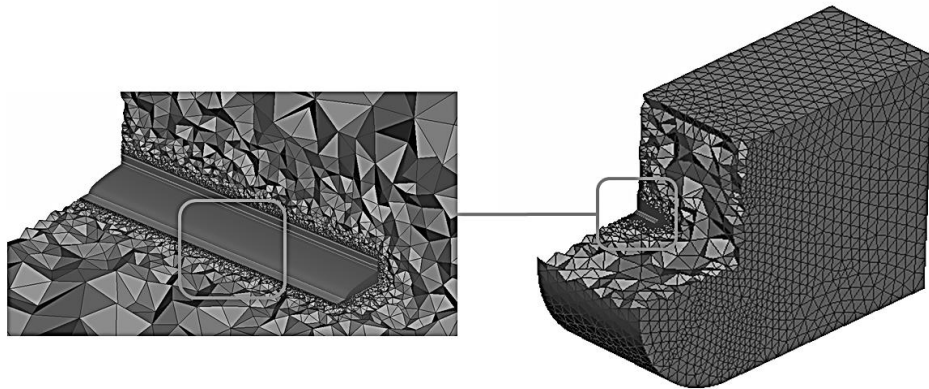


Figure 38. Flow domain used for the simulations of the 3D NACA 65-009 wing

The contour plots of the flow properties of the three-dimensional flow domain given from Figure 39 to Figure 47 are compared for different free stream velocities. The upper and the lower fin surfaces are demonstrated separately in these figures.

According to the results, it is seen that an increase in flow speeds causes an increase in the amount of energy transformation from the kinetic energy to the heat energy. Also a smaller shock wave distance at the leading edge is formed by increasing the

flow speed. Therefore, the values of temperature near the leading edge are increased more than the other part of the wing. These values become important when the free stream velocity is reached Mach 2.

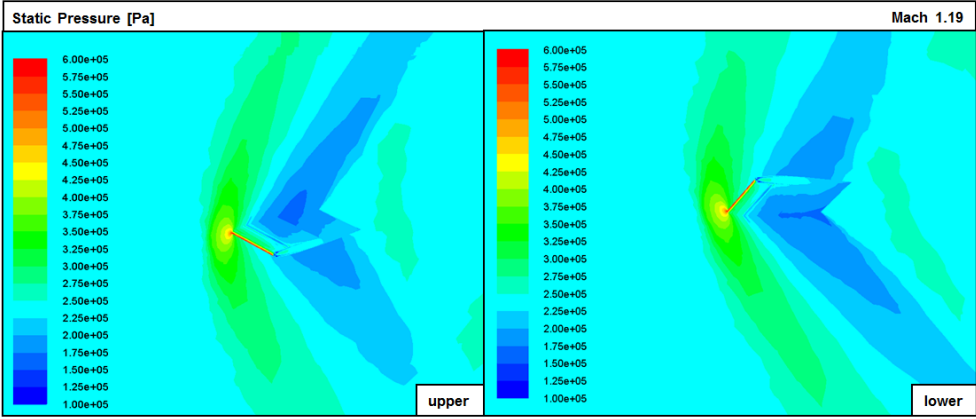


Figure 39. Static pressure contours for Mach 1.19 (3D-Clean wing conf.)

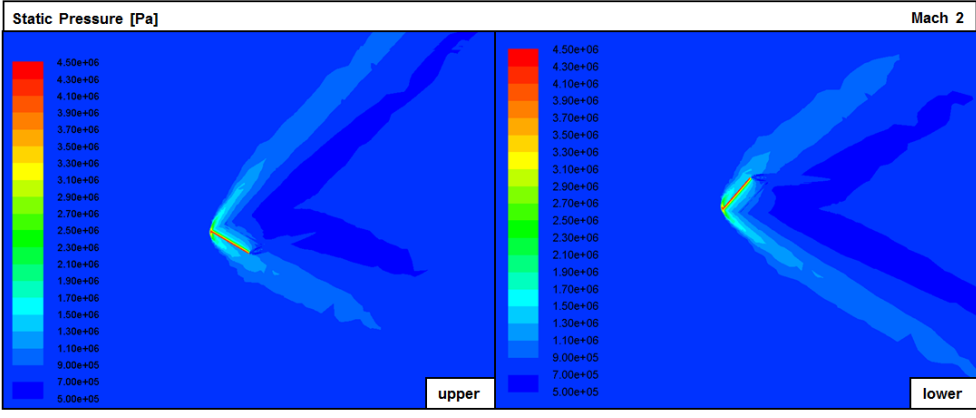


Figure 40. Static pressure contours for Mach 2 (3D-Clean wing conf.)

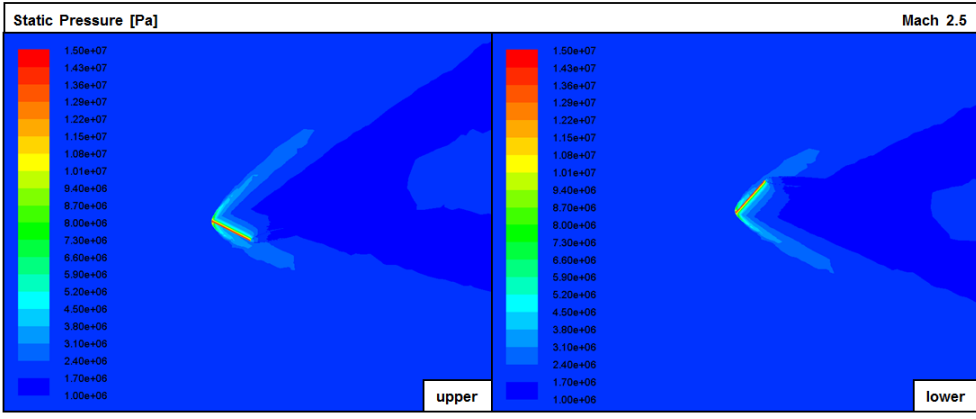


Figure 41. Static pressure contours for Mach 2.5 (3D-Clean wing conf.)

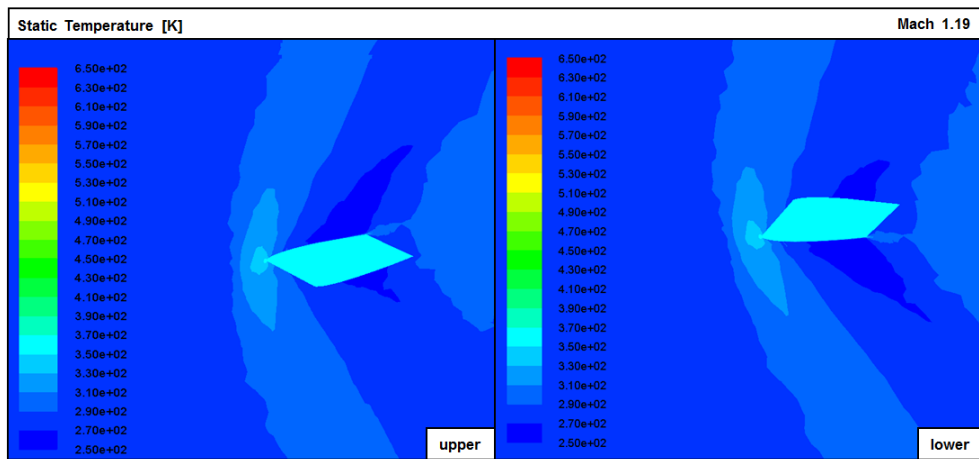


Figure 42. Static temperature contours for Mach 1.19 (3D-Clean wing conf.)

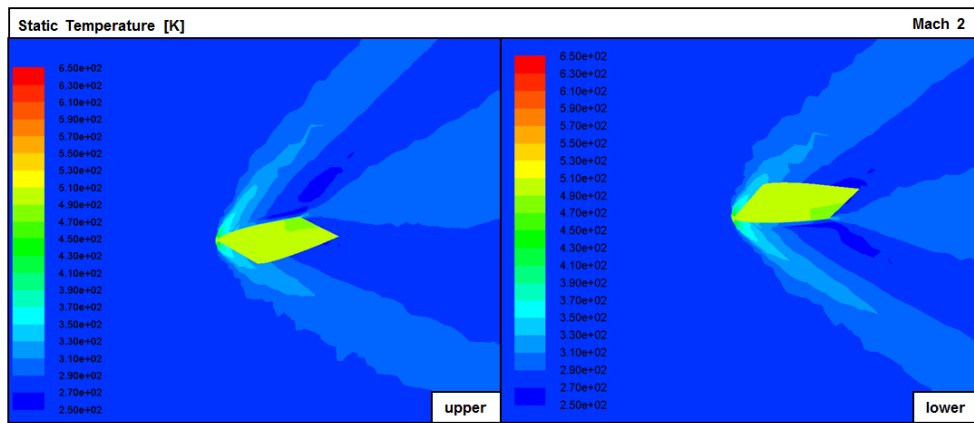


Figure 43. Static temperature contours for Mach 2 (3D-Clean wing conf.)

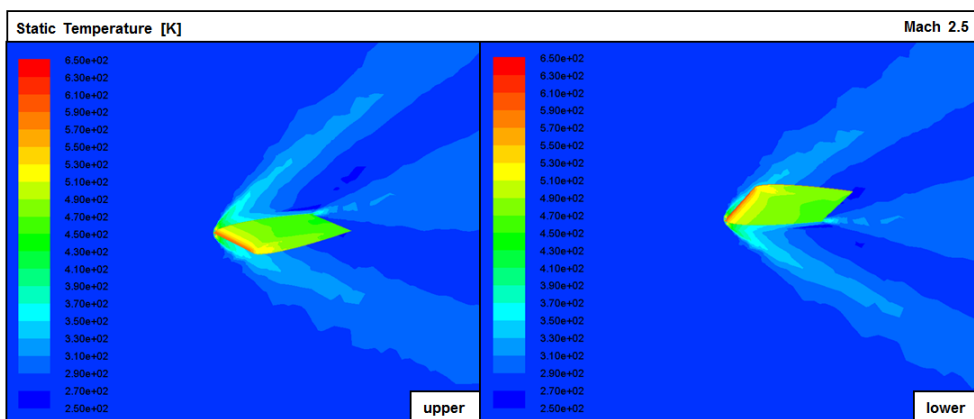


Figure 44. Static temperature contours for Mach 2.5 (3D-Clean wing conf.)

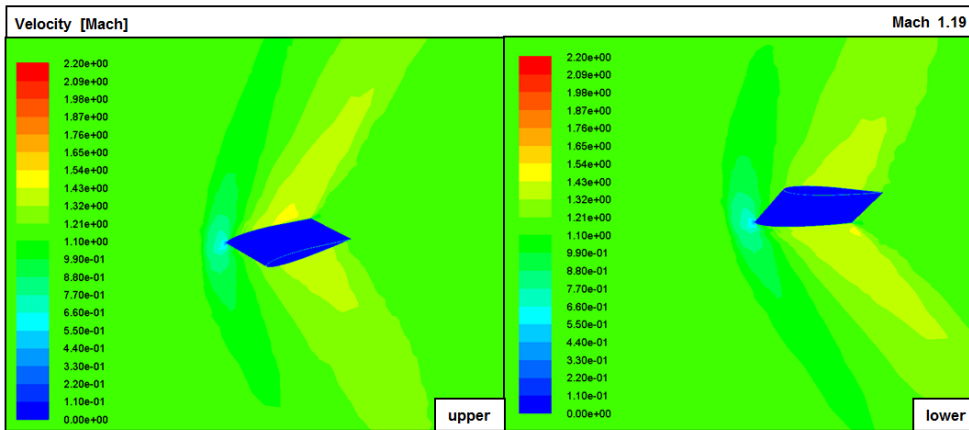


Figure 45. Mach number contours for Mach 1.19 (3D-Clean wing conf.)

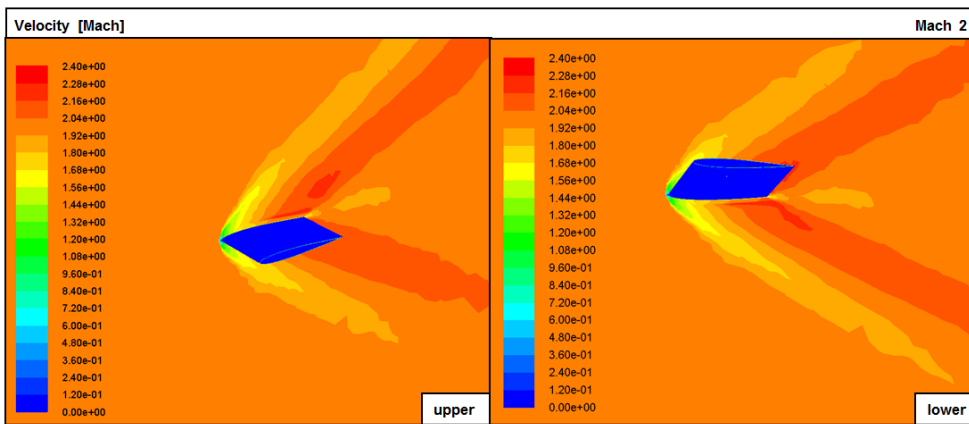


Figure 46. Mach number contours for Mach 2 (3D-Clean wing conf.)

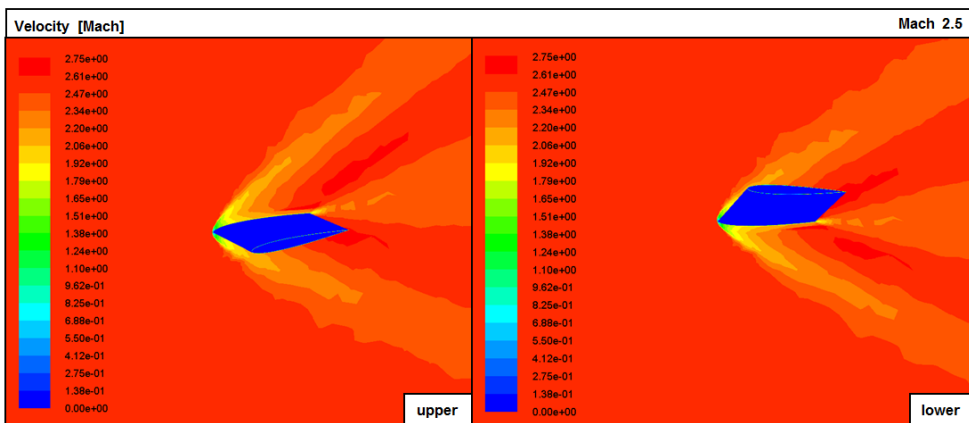


Figure 47. Mach number contours for Mach 2.5 (3D-Clean wing conf.)

The pressure distribution around the wing body is localized by increasing the free stream velocity. Due to the compression of the high speed flow, the pressure values get changed rapidly.

The variations of the total drag coefficient with the free stream velocities are presented in Figure 48. It is clearly seen in the figure that the drag coefficient is decreasing with the free stream velocity. By modelling the fin in three-dimensional form, the difference between the numerical simulation and the test data is decreased from 8.5% to 6.4%. In Figure 49 and Figure 50, the pressure coefficient distributions along chord at 33% and 67% span are shown. The values of the pressure coefficient decreases by increasing the free stream velocity. The pressure distribution is similar at upper and lower wing surfaces for the both sections at 33% and 67% span.

Figure 51 shows that the maximum wall temperature and static pressure on the fin varies with the free stream velocity. The maximum temperature and pressure values for all free stream velocities are placed on the leading edge.

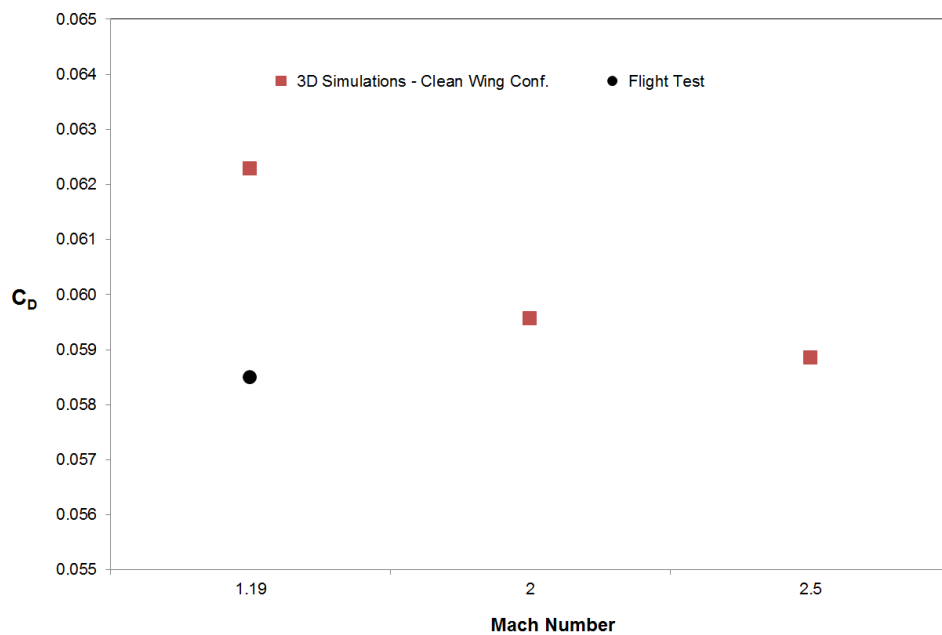


Figure 48. Drag coefficients for different free stream velocities (3D-Clean wing conf.)

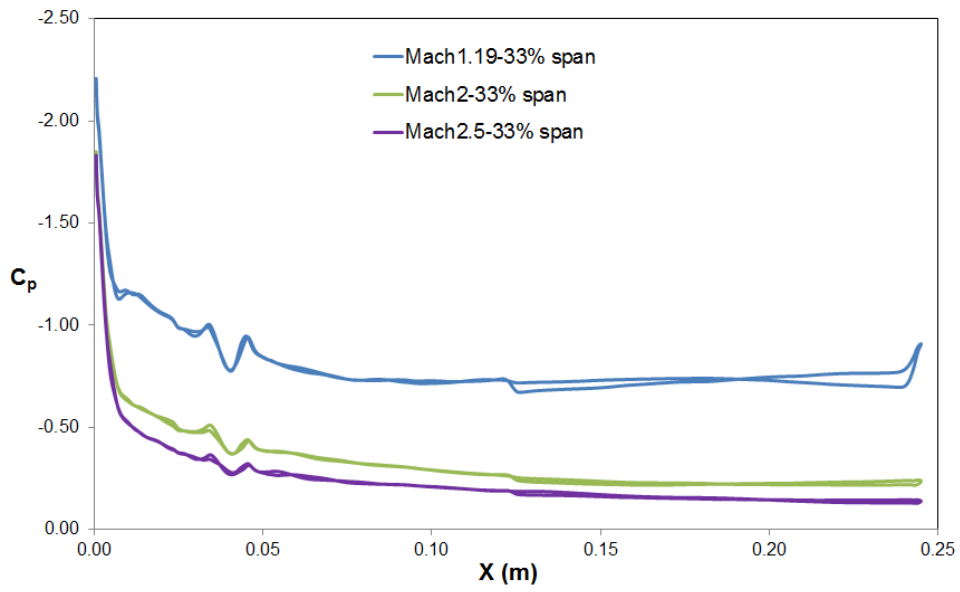


Figure 49. C_p distribution at 33% wing span (3D-Clean wing conf.)

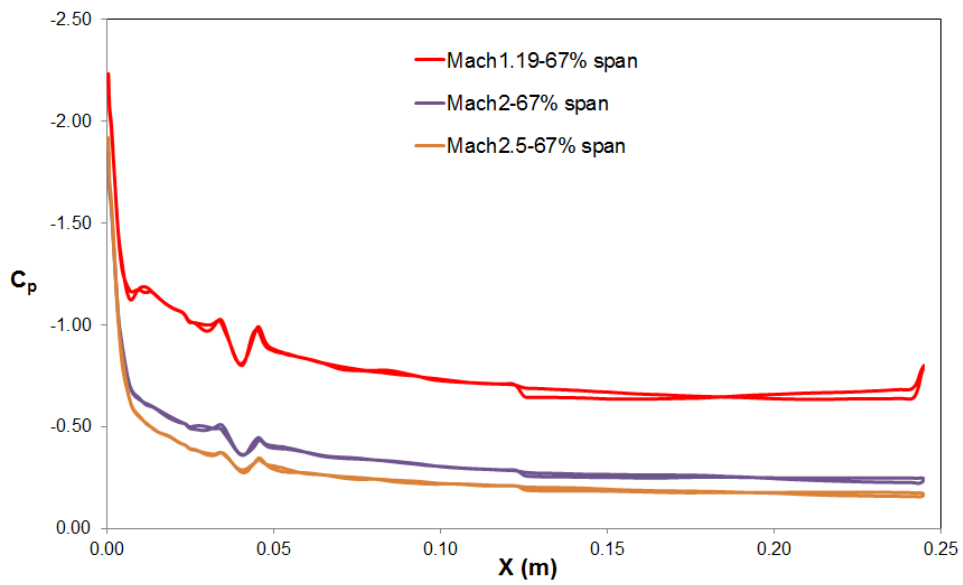


Figure 50. C_p distribution at 67% wing span(3D-Clean wing conf.)

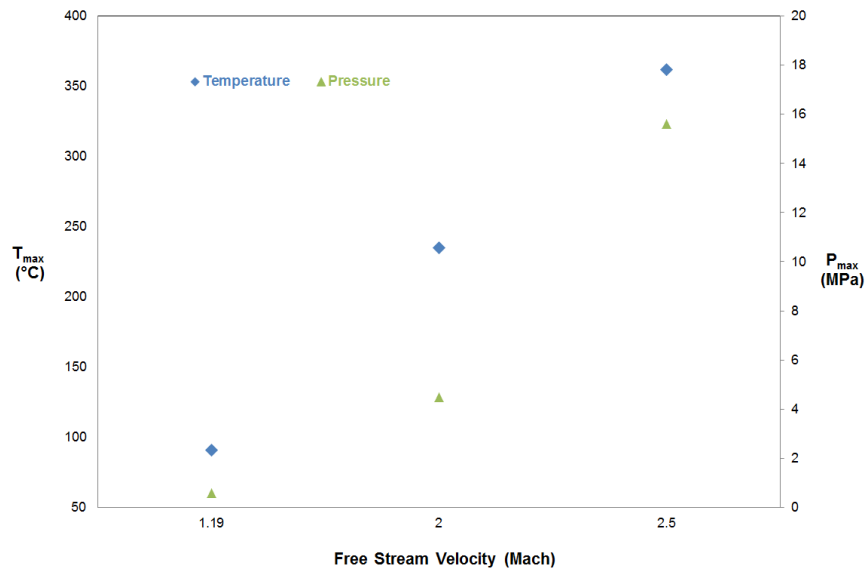


Figure 51. Variation of the maximum temperature and pressure on the wing surface

In order to solve the structural deformation, the external loads from the flow simulation are transferred to the FE model given in Figure 52. In the FE simulation of this configuration, the external loads are mapped to only the wetted surface on the wing as shown in Figure 53.

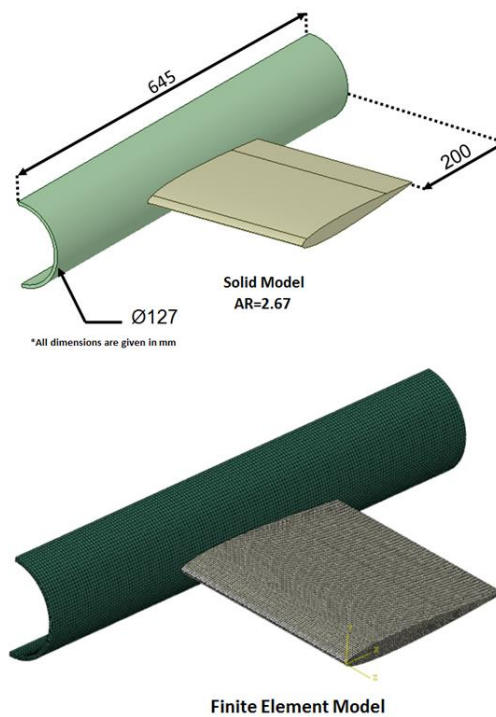


Figure 52. The FE model used to obtain the structural deformation

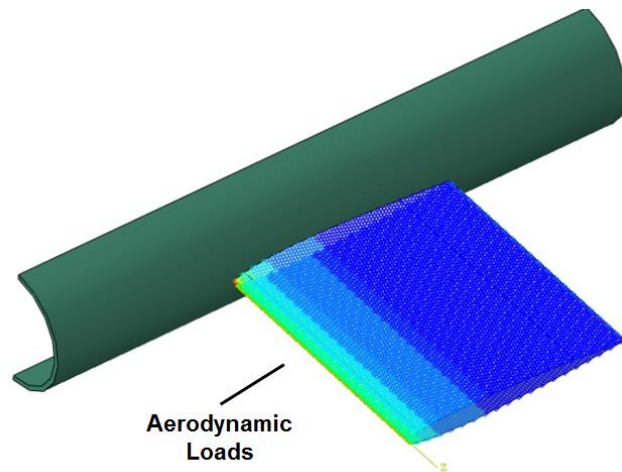


Figure 53. External loads applied on the FE model

The maximum wing displacement changes with the flow speed and it is shown in Table 6. According to the Table 6, the deformation on the fin/body configuration calculated by using the external loads obtained from the free stream Mach 1.19 and 2 are relatively small and considered to be negligible. Therefore, the deformation is modelled only for the case for the free stream Mach 2.5. Figure 54 shows the deformations for the free stream Mach 2.5.

Table 6. Deformations on wing body for different Mach number

Free Stream Velocity (Mach)	Max. Deformation on Wing Tip (mm)
1.19	0.34
2	1.22
2.5	3.85

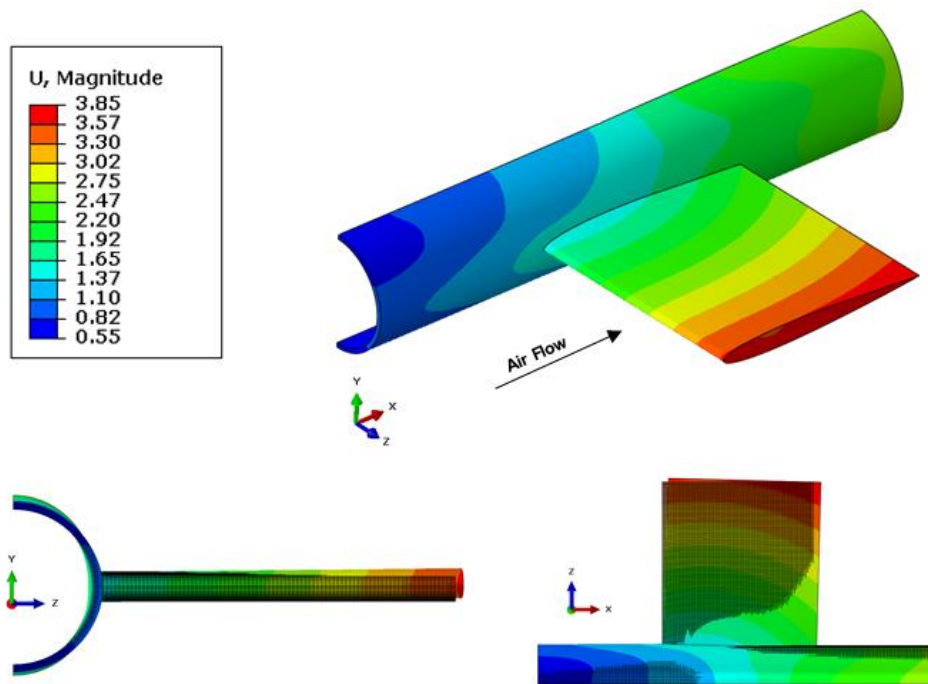


Figure 54. Deformation contours on wing body for Mach 2.5 (mm)

In order to investigate the effect of deformation, the flow simulation is repeated with the deformed wing model obtained from the FE simulation. In Abaqus r6.13, the deformed grid could be exported as the orphan mesh that includes only the grid information without any geometrical data. The deformed model is used for reproducing the flow domain.

Figure 55 shows the comparison of the flow domain of the deformed and the undeformed model for the free stream Mach 2.5. After modelling the flow domain with the deformed wing, the CFD simulation is conducted with the same solution setup used for the undeformed simulation.

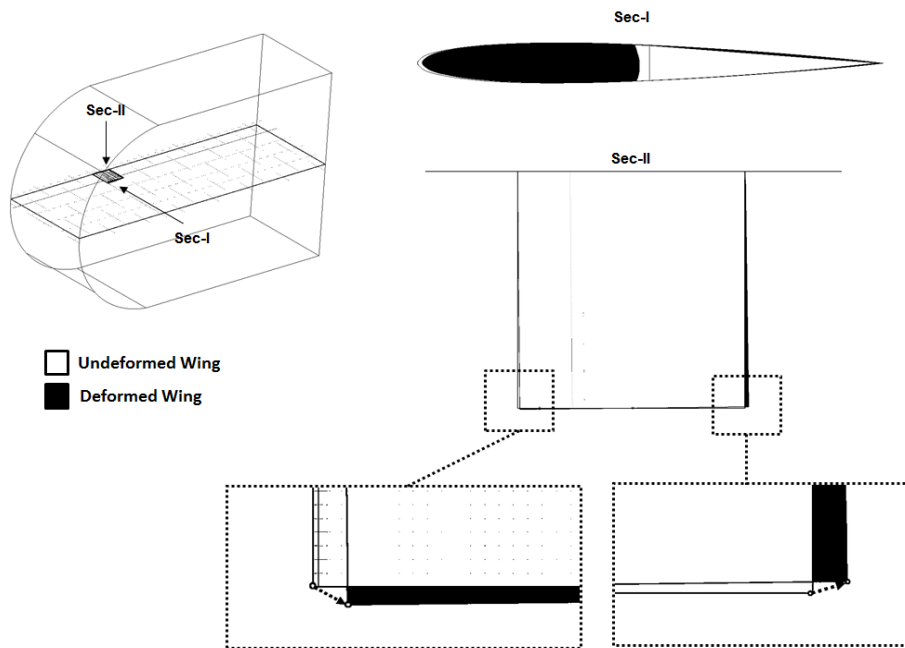


Figure 55. Deformed and undeformed wing CFD model for Mach 2.5

The effect of the deformation on the drag coefficient is demonstrated in Table 7. As shown in Table 7, the wing drag coefficient is increased with deformation by 5.1%.

The pressure coefficient distribution is presented at 33% span and 67% span in Figure 56. According to this figure, the pressure coefficient along the chord obtained for the deformed body is more than that obtained for the undeformed wing body. This difference explains the increasing in the aerodynamic coefficients.

From the solution of the deformed CFD simulations, the aerodynamic coefficients are calculated to compare the effect of the deformation on the aerodynamic performance. The flow properties of the deformed and the undeformed wings are compared between Figure 57 and Figure 59 are compared to the results of undeformed wing. According to these figures, temperature and Mach number distributions around the leading edge has a small difference because of the wing deformation.

Table 7. Wing drag coefficient (C_D) for deformed and undeformed wing

	Undeformed Wing	Deformed Wing	Percent Change [%]
C_D	0.059	0.062	5.1

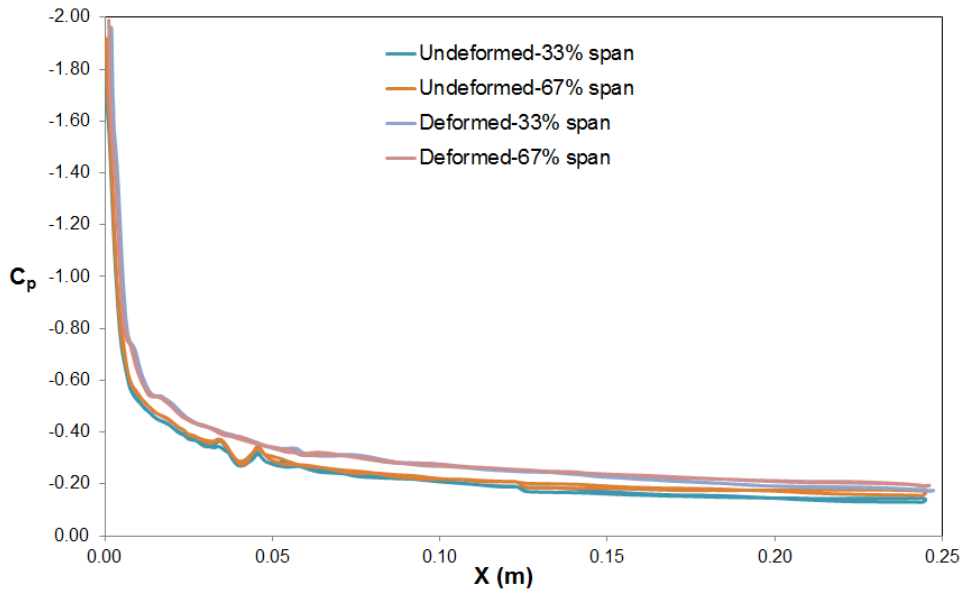


Figure 56. C_p distribution for undeformed wing at 33% and 67% span

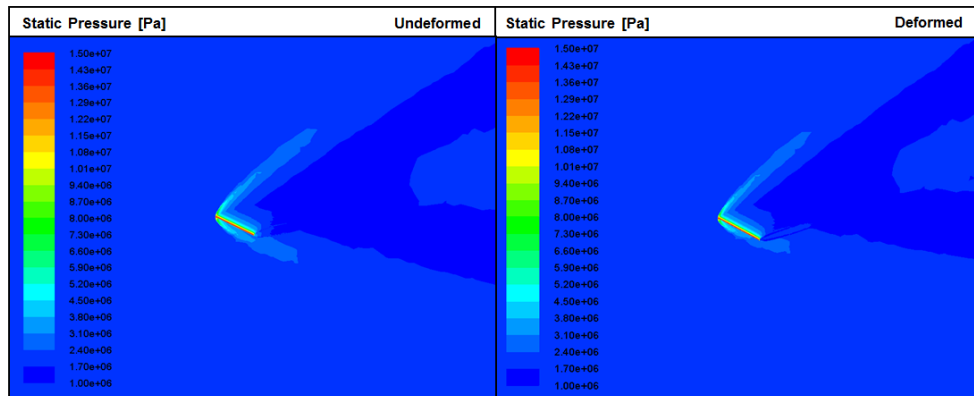


Figure 57. Static pressure contours of undeformed and deformed wings ($M=2.5$)

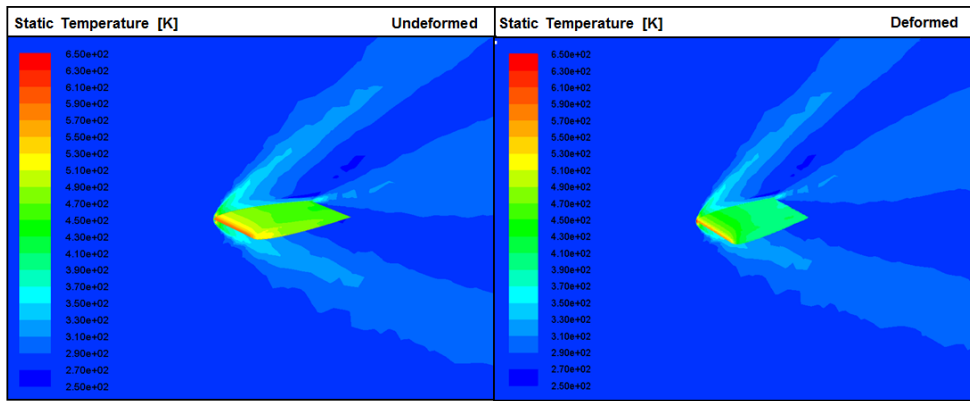


Figure 58. Static temperature contours of undeformed and deformed wings(M=2.5)

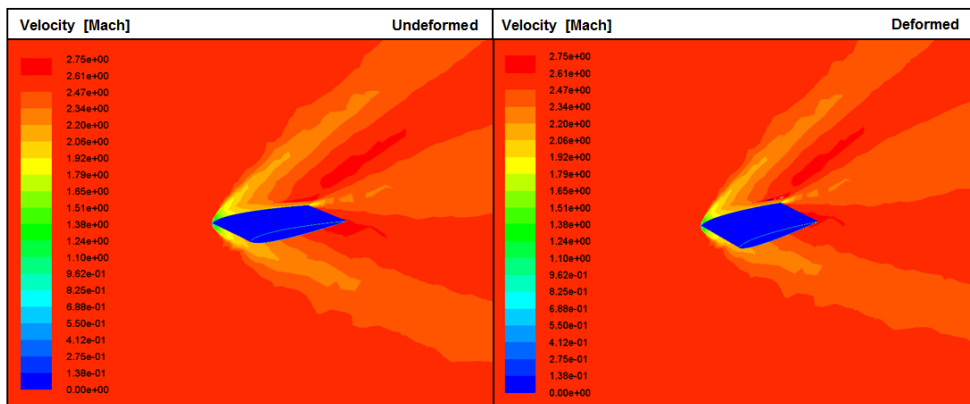


Figure 59. Mach number contours of undeformed and deformed wings(M=2.5)

4.3. Simulations for the Missile Equipped with 3D NACA65-009 Wing

The two and three-dimensional flow problems are investigated in Chapter 4.1 and Chapter 4.2. According to these simulations, the behavior of the flow on the wing surface is predictable. By the way, the model used includes only the wing section, so these results are only valid for the flow properties around the wing section.

In this chapter, the effect of the missile body and the body-wing interaction on the flow characteristics is incorporated into the flow problem. The same procedure given in Figure 6 is followed in order to obtain the effect of deformation.

In the CFD simulations discussed in this chapter, the missile and the wing bodies are modelled in detail. In order to solve the flow problem, the flow domain given in Figure 60 is used. The medium level mesh for the missile and the wing bodies demonstrated in Chapter 3.2.1 is used. The boundary layer is modelled in all fluid-

solid interaction surfaces. The solid region is also meshed in order to perform the conjugate heat transfer problem.

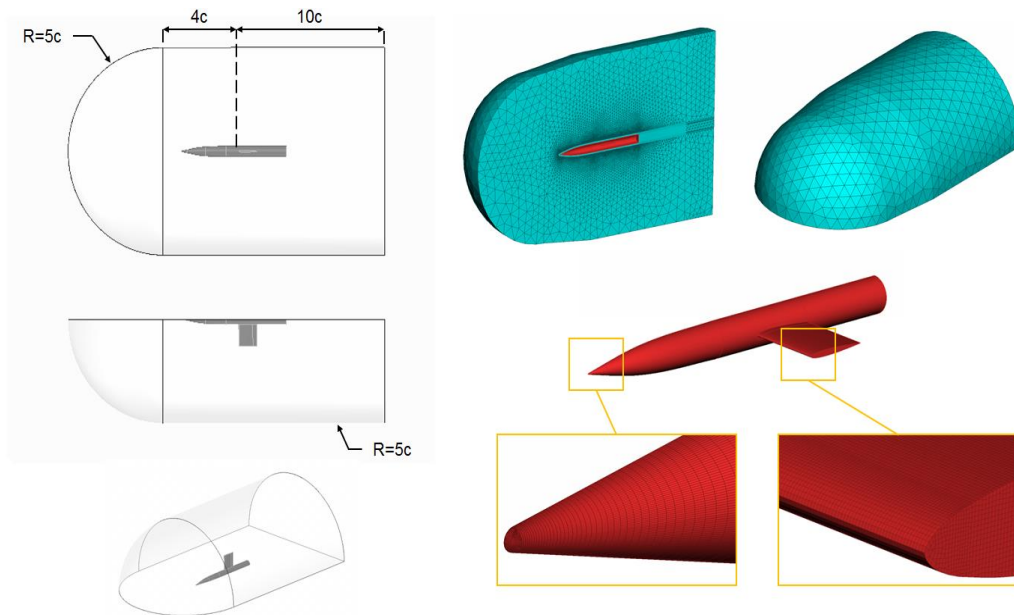


Figure 60. Flow domain for the missile equipped with NACA65-009 wing

The CFD simulations are carried out for the three different free stream velocities. The solver setup remains the same as those in the simulations given in Chapter 4.2. The contours of the flow properties are shown between Figure 61 and Figure 69. According to the results, the solution of the flow problem around the wing is similar to the solution given in Chapter 4.2 except the wing root region. In this region, there are local sections that the wall temperature is hot due to the stagnation of the flow.

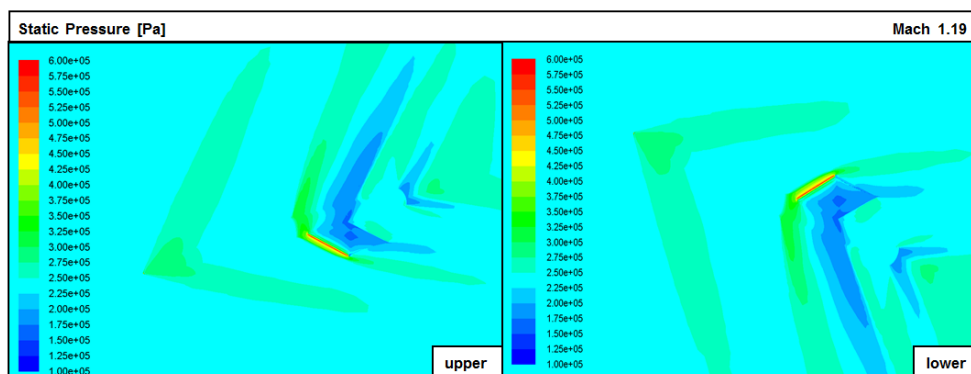


Figure 61. Static pressure contours for Mach 1.19 (3D-Full model conf.)

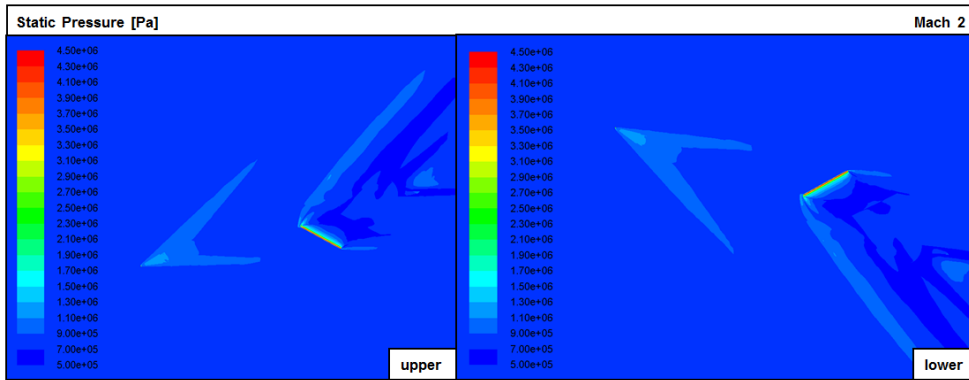


Figure 62. Static pressure contours for Mach 2 (3D-Full model conf.)

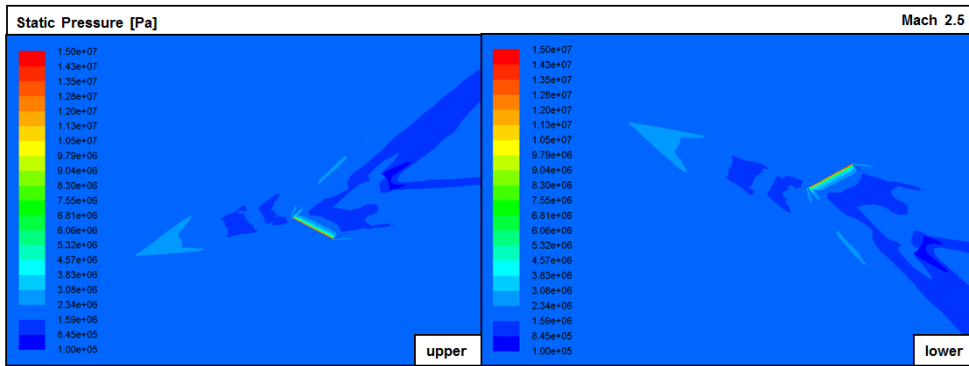


Figure 63. Static pressure contours for Mach 2.5 (3D-Full model conf.)

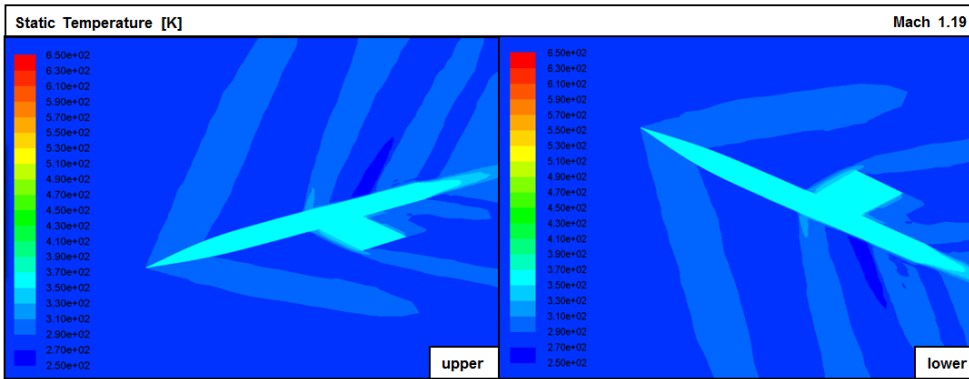


Figure 64. Static temperature contours for Mach 1.19 (3D-Full model conf.)

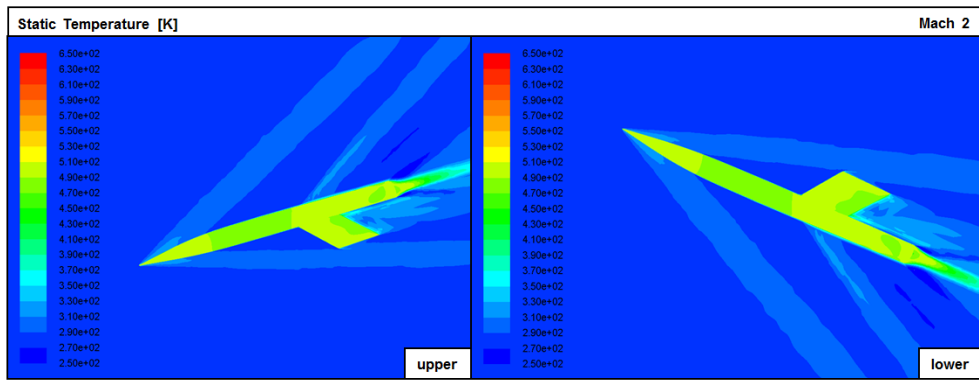


Figure 65. Static temperature contours for Mach 2 (3D-Full model conf.)

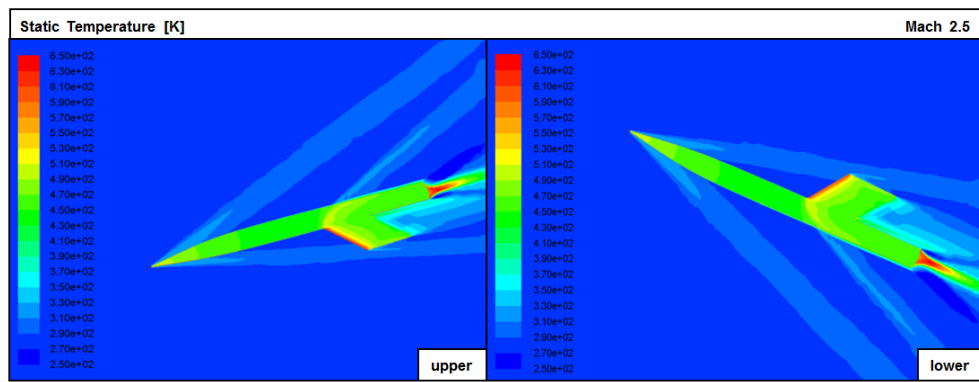


Figure 66. Static temperature contours for Mach 2.5 (3D-Full model conf.)

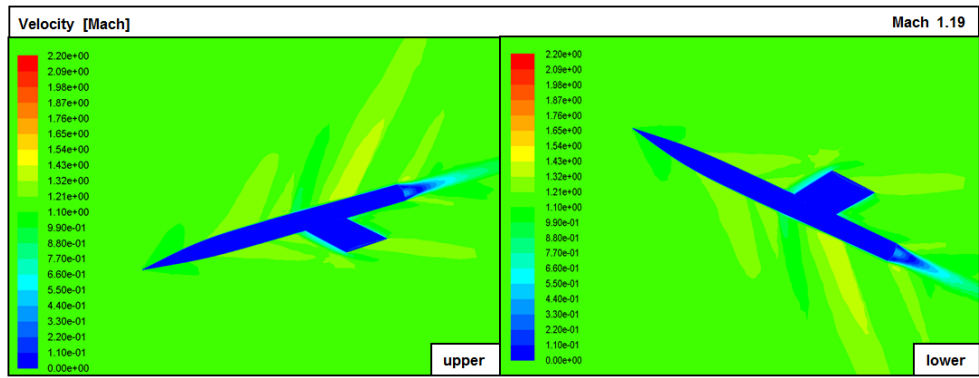


Figure 67. Mach number contours for Mach 1.19 (3D-Full model conf.)

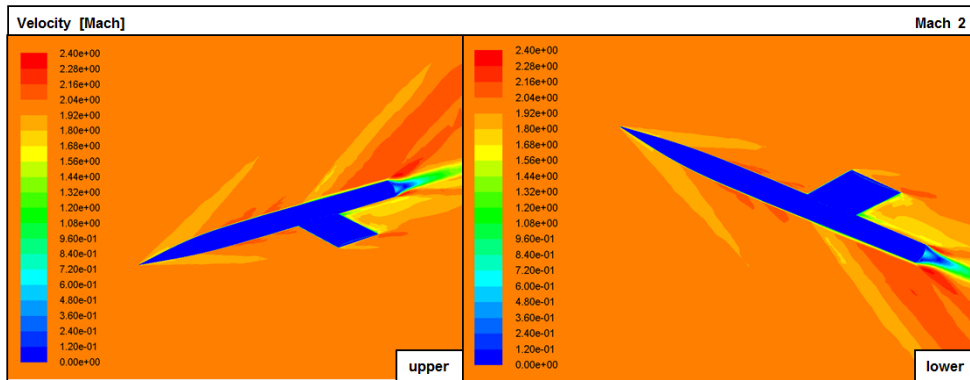


Figure 68. Mach number contours for Mach 2 (3D-Full model conf.)

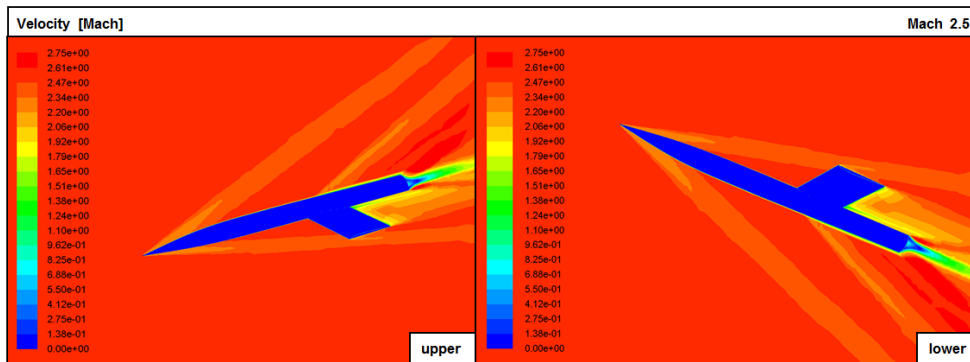


Figure 69. Mach number contours for Mach 2.5 (3D-Full model conf.)

The wing drag coefficient is calculated at each free stream velocities and the variation is plotted in Figure 70. Figure 70 shows that the missile body is affected to the wing drag coefficient because the difference between the wing drag coefficient obtained from the numerical simulation and that obtained from the flight test is decreased to 1.7%. Thus, more realistic solution is obtained for the flow problem.

In Figure 71 and Figure 72, pressure coefficient distributions along chord at 33% and 67% span are shown. The pressure coefficient is distributed similarly at upper and lower wing surface; therefore, no lift is obtained on the wing body. It is seen in Figure 71 and Figure 72 that small oscillations could be occurred because of the increase in the instability at the region behind the shock wave.

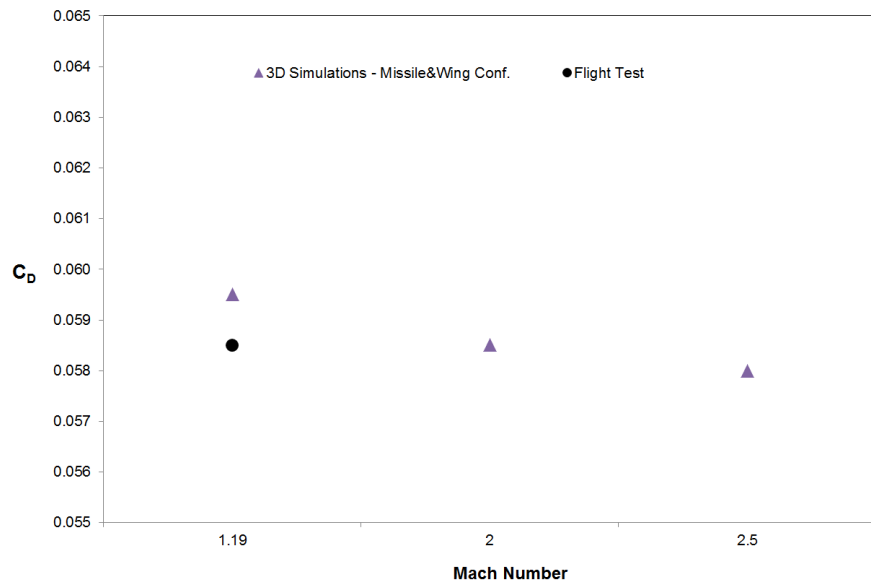


Figure 70. Drag coefficients for different free stream velocities (3D-Missile&Wing Conf.)

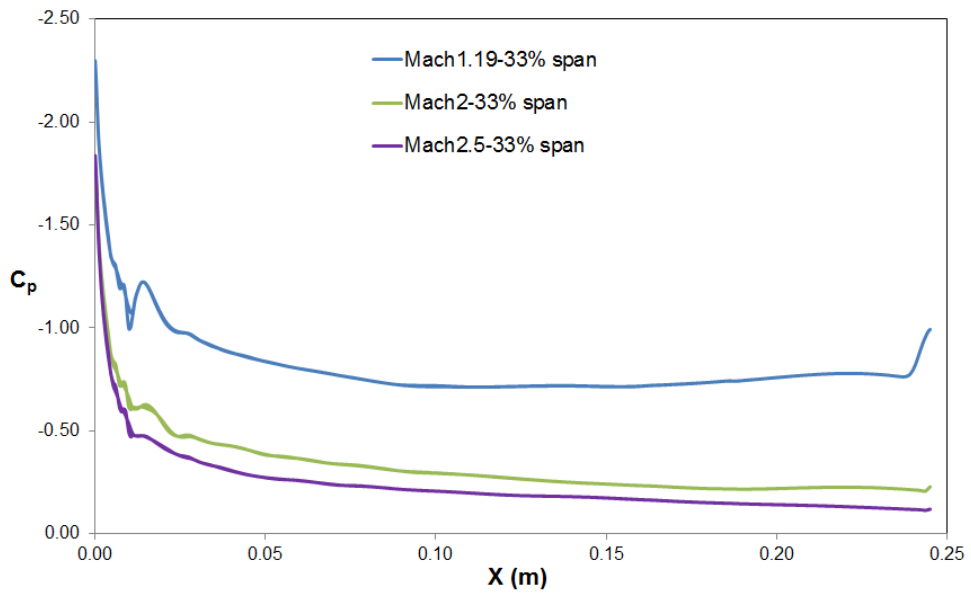


Figure 71. C_p distribution at 33% wing span (3D-Missile&Wing Conf.)

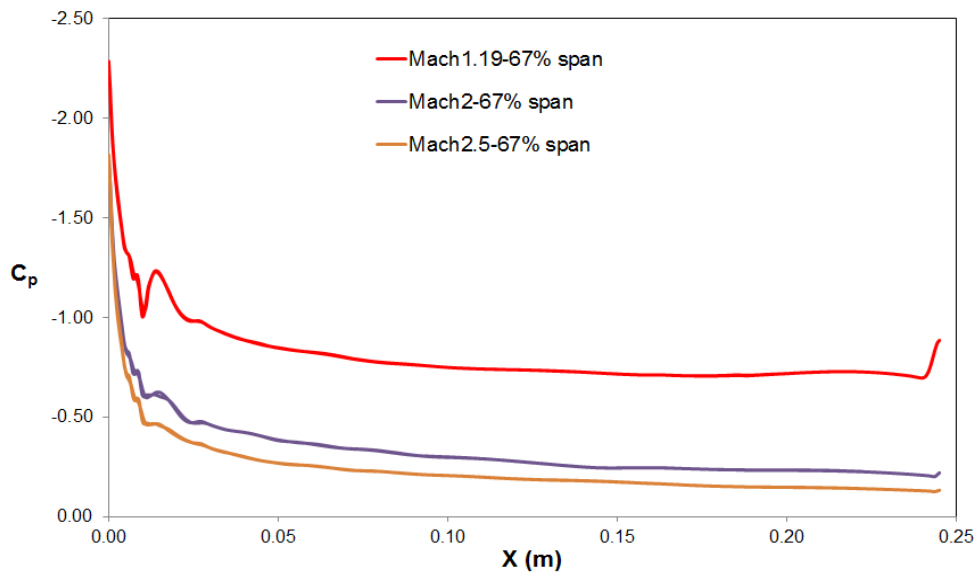


Figure 72. C_p distribution at 67% wing span (3D-Missile&Wing Conf.)

The maximum wall temperature on the wing is obtained on the leading edge at the wing root section. The change of maximum wall temperature and pressure with different free stream velocities are demonstrated in Figure 73. The missile body has a small effect on the maximum wall temperature of the leading edge. Because the values of wall temperature and pressure values given in Figure 73 is quite similar to those values given in Figure 51.

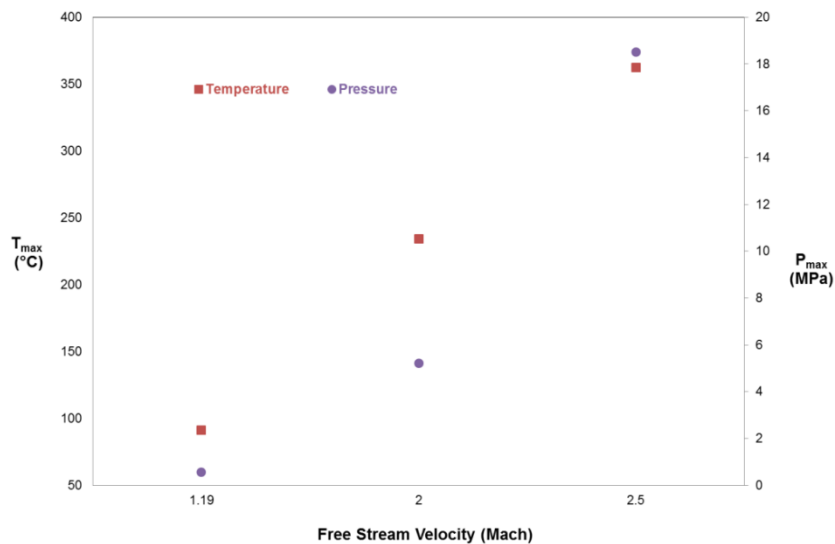


Figure 73. Variation of maximum temperature and pressure on the wing surface

The external loads obtained from the solution of the CFD simulations are transferred to the FE simulations. The FE simulations are conducted by the FE model given in Figure 74. In the FE model, the external loads are applied to the missile body in addition to the wing surfaces. Figure 75 demonstrates the boundary conditions applied. In Chapter 3.1.2, the simulation technique and the solver setup used in Abaqus Standard are given in detail.

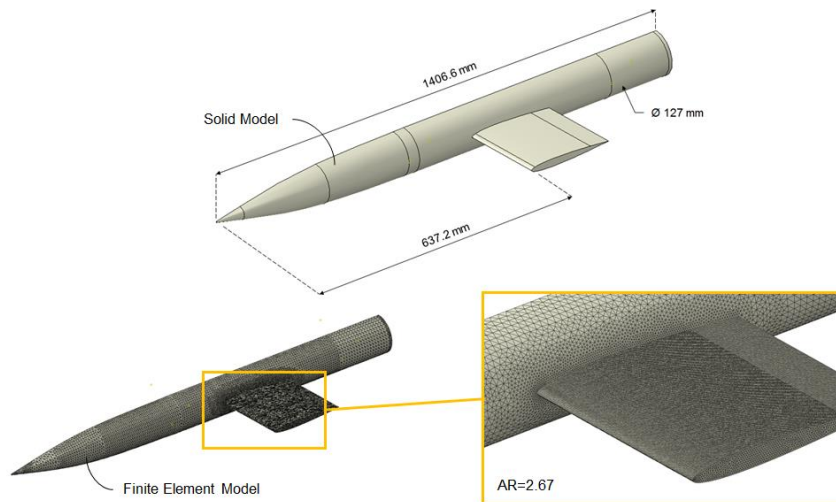


Figure 74. Finite element model of the missile with NACA wing

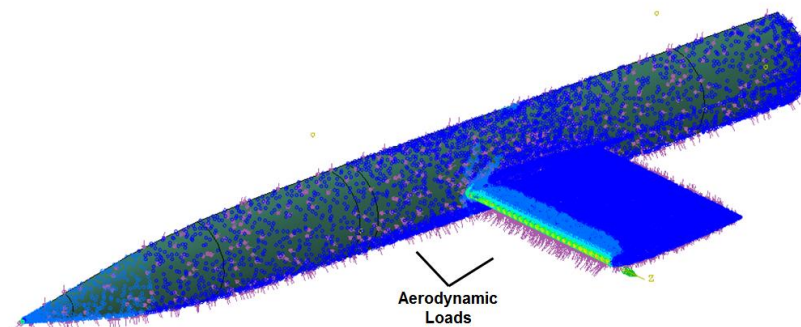


Figure 75. External loads applied on the FE model of the missile with NACA wing

Table 8. Deformations on the wing body for different Mach number

Free Stream Velocity (Mach)	Max. Deformation on the Wing Tip (mm)
1.19	0.62
2	2.03
2.5	3.96

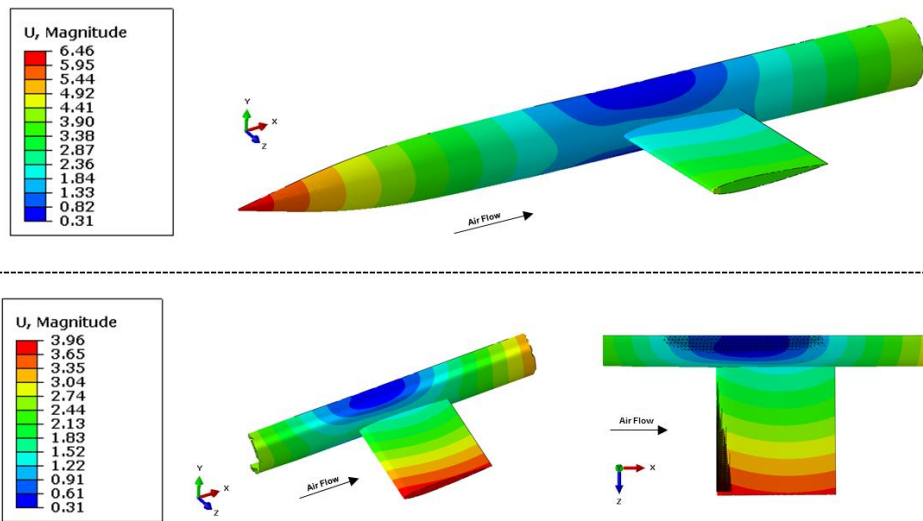


Figure 76. Deformations of deformed body at free stream Mach number of 2.5

The results of the FE simulations given in Table 8 show that the maximum deformation on the FE model is placed on the missile nose and the wing tip and the maximum wing displacement changes with the free stream velocity.

According to the results, the wing tip deformation for the free stream Mach 1.19 and 2 are relatively small; so, it is neglected. For the case of the free stream Mach 2.5, the maximum wing tip deformation is used for investigating the effect of the deformation. Figure 76 shows the deformations on the missile body and wing at the free stream Mach 2.5.

The deformed model that includes the deformed wing and the deformed missile body is modelled in order to recreate the flow domain. The deformation modelling process is the same as that given in Chapter 4.2; so, the detail of the deformation modelling is not given in that section.

After solving the flow problem with the deformed body, the flow properties are calculated for the same region as that in the simulation of the deformed model. The comparisons of the flow properties around the wing body for the deformed and undeformed simulations are made between Figure 77 and Figure 79. According to these figures that there is a little difference on the shock wave on the static pressure and static temperature contours, so this difference cause that the aerodynamic loads on the deformed wing differ from the loads on the undeformed wing., The aerodynamic performance of the wing is changed due to this difference. Table 9 shows that the aerodynamic performance of the wing is changed 8.6% by deformation.

Table 9. Wing drag coefficient (C_D) for deformed and undeformed wing - 2

	Undeformed Wing	Deformed Wing	Percent Change [%]
C_D	0.058	0.063	8.6

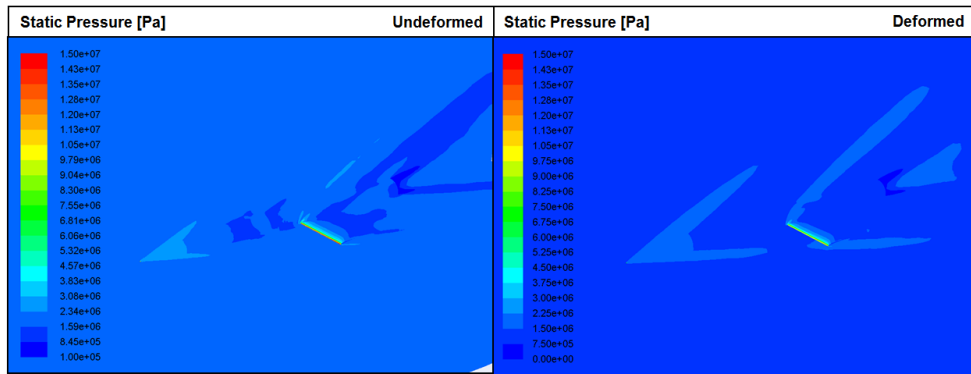


Figure 77. Static pressure contours of undeformed and deformed wings ($M=2.5$)

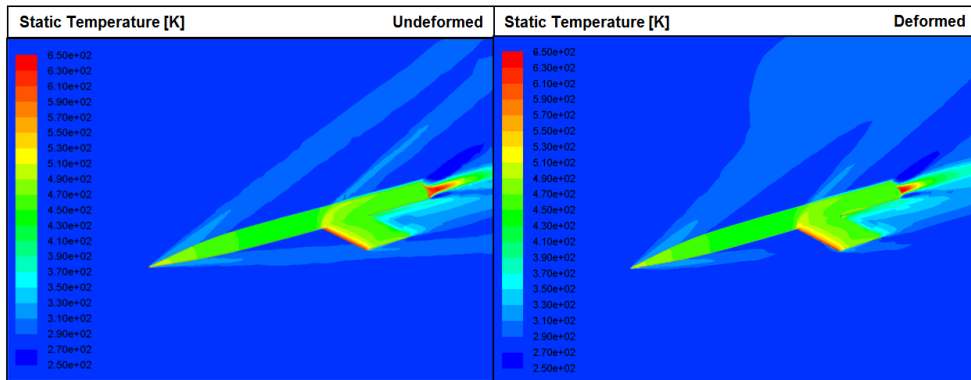


Figure 78. Static temperature contours of undeformed and deformed wings (M=2.5)

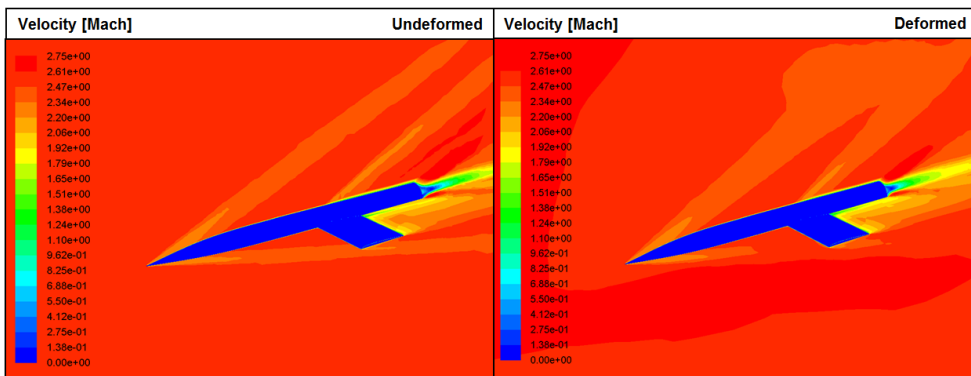


Figure 79. Mach number contours of undeformed and deformed wings (M=2.5)

The pressure coefficient distribution is presented at 33% span and 67% span in Figure 80. It is seen in Figure 80 that, the difference in the pressure coefficient variations of deformed and undeformed wing is increased relative to the difference given in Figure 56. The main reason of the change in the aerodynamic performance is this difference.

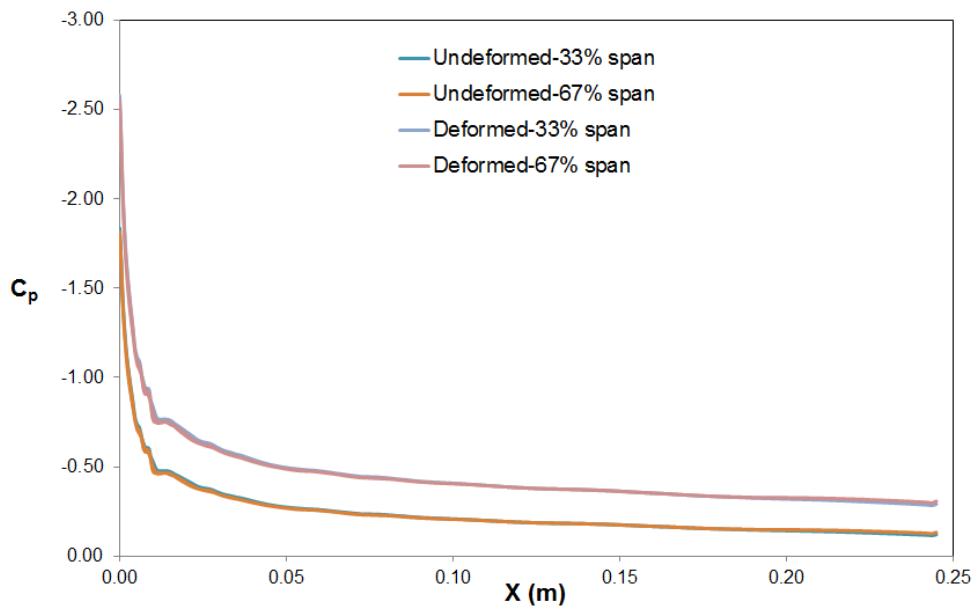


Figure 80. C_p distribution for undeformed wing at 33% and 67% span

CHAPTER 6

CONCLUSION

In order to obtain to the effect of the wing deformation due to the aerothermal loading on the aerodynamic performance, the methodology given in Chapter 2.2 is used. Two and three-dimensional simulations are performed for the method validations and the real case applications. A missile equipped with NACA-65-009 wings from the study of Alexander (1947) is considered to be the validation model of the simulations.

The flow characteristics around the airfoil are aimed to be obtained from two-dimensional simulations of this study. The change in the aerodynamic loads for three different free stream velocities is obtained.

In order to simulate the three-dimensional effect, the flow domain is modelled in three-dimensional. The results of these simulations are shown that the wing tip is deformed more than the other sections of the wing and the deformation on the wing become important when the free stream velocity reaches to Mach number of 2.5. The difference in the aerodynamic performance between the deformed and the undeformed wing is about 5.1%.

In the second part of three-dimensional simulations, a missile equipped with NACA 65-009 wings from the study of Alexander (1947) is modelled. It is aimed that the effect of the missile body on the flow characteristics are obtained. The deformations obtained for the missile body and the wing are demonstrated in the Chapter 4. The aerodynamic performance of the deformed wing changes by 8.6% compared to that for the undeformed wing.

The studies carried out by using the method demonstrated in this thesis study are presented in three different conferences. In the preliminary phase of this study, it is aimed to construct the structure of the method. NACA0012 airfoil is selected as the validation case. The results of these simulations are compared with the wind tunnel

test data of NACA0012 airfoil and the outcomes are presented in two different studies of Ozkokdemir et al. (2016). The studies for NACA0012 airfoil are excluded the scope of this thesis in order to ensure that the integrity of the subject is not impaired. The method used is applied to the study of Alexander (1947) that is a flight test of a missile equipped with NACA 65-009 wings with experiences obtained from the preliminary phase of this study. The results are presented in another study of Ozkokdemir et al. (2017). Consequently, the method used is verified by various tests from the wind tunnel to the flight.

As a future work, the method used could be applied to other experimental studies. It could be investigated how the flow conditions changed with the deformation affect the mechanical integrity of the wing. Also the method could be improved by modelling the body deformation in fully-coupled simulations

REFERENCES

- Abbott, I.H., Von Doenhoff, A.E. (1945). *Summary of Airfoil Data*. NACA Report 824.
- Alexander, S. (1947). Drag Measurements of Symmetrical Circular-arc and NACA 65-009 Rectangular Airfoils Having an Aspect Ratio of 207 as Determined by Flight Tests at Supersonic Speeds. *NACA Research Memorandum*.
- Alexander, S.R, Katz, E. (1947). Drag Characteristics of Rectangular and Swept-Back NACA 65-009 Airfoils Having Aspect Ratios of 1.5 and 2.7 as Determined by Flight Tests at Supersonic Speeds. *NACA Research Memorandum*.
- Anderson, J. D. (2017). *Fundamentals of Aerodynamics*. New York: McGraw Hill Education.
- ANSYS Inc. (2013). *Fluent r15 User & Theory Guide*. Canonsburg: ANSYS.
- Borovoy, V.Y., Kubyshina, T.V. (1993). Hypersonic Heat Transfer on the Upper Wing Surface Fins. *AIAA/DGLR 5th International Aerospace Planes and Hypersonic Technologies Conference*.
- Callister, W. (2007). *Materials Science and Engineering: An Introduction*. Wiley & Sons Inc.
- DS Simulia Corp. (2013). *Abaqus r6.13 Standard User & Theory Guide*. Dassault Systèmes.
- Eleni D. C., Athanasios T.I. . (2012). Evolution of the turbulence models for the simulation of the flow over a NACA 0012 airfoil. *Journal of Mechanical Engineering Research*.
- Ericsson, L.E., Almroth, B.O., Bailie, J.A. (1978). Hypersonic Aerothermoelastic Characteristics of a Finned Missile. *AIAA 16th Aerospace Sciences Meeting*.
- Giles, D.M., Marshall, D.D. (2008). Aerodynamic Performance Enhancement of a NACA 66-206 Airfoil Using Supersonic Channel Airfoil Design. *AIAA 46th AIAA Aerospace Sciences Meeting and Exhibit*.
- Hoffman, J., Jansson, J., Jansson, N. (2016). *Simulation 3D Unsteady Incompressible Flow Past a NACA 0012 Wing Section*. Computational Technology Laboratory Report.

- Johansen, J. (1997). *Prediction of Laminar/Turbulent Transition in Airfoil Flows*. Risø National Laboratory.
- Kayabasi, I., Akgul, A., Kurtulus, D.F. (2012). NACA0012 Kanat Profili için Sinusoidal Yunuslama Hareketinin Hesaplamalı Akışkanlar Dinamiği ile Modellenmesi. *IV. Ulusal Havacılık ve Uzay Konferansı*.
- Kurtulus, D. (2005). Numerical and Experimental Analysis of Flapping Motion in Hover. Application to Micro Air Vehicles. *Joint Ph.D thesis Poitiers University/ENSMA (Poitiers-France) and METU (Ankara-Turkey)*.
- Kurtulus, D. (2015). On the Unsteady Behavior of the Flow Around NACA 0012 Airfoil with Steady External Conditions at $Re=1000$., *International Journal of Micro Air Vehicles*, 301-326.
- Lillard, R. (2011). *Turbulence Modelling for Shock Wave/Turbulent Boundary Layer Interactions*. Indiana: Purdue University.
- Martinat, G., Braza, M., Hoarau, Y., Harran, G. (2008). Turbulence Modelling of the Flow Past a Pitching NACA 0012 airfoil at 105 and 106 Reynolds Number. *Journal of Fluids and Structures*.
- Michel, R. (1958). *Etude de la Transition sur les Profils d'Aile; Etablissement d'un Critère de Determination de Point de Transition et Calcul de la Trainee de Profile Incompressible*. ONERA Report.
- Ozkokdemir, E., Acar, B., Kurtulus, D.F. (2016). Termal Yüklere Maruz Kalan NACA 0012 Kanat Yapısının İncelenmesi. *Savunma Teknolojileri Kongresi*. Ankara.
- Ozkokdemir, E., Kurtulus, D.F. (2016). Investigation of the Mechanical Integrity of Wings/Fins under Thermal Loading. *9th International Conference on Computational Fluid Dynamics, ICCFD9*. Istanbul.
- Ozkokdemir, E., Kurtulus, D.F. (2017). Effect of Wing Deformation On Aerodynamic Loads At Supersonic Speeds. *Ankara International Aerospace Conference*. Ankara.
- Polli, G.M., Mastroddi, F., Librescu, L. (2008). Aerothermoelastic Stability of Composite Aerovehicle Wings Subjected to Heat Inputs. *AIAA Journal Vol. 46*.
- Rodgers, J. (1992). Aerothermoelastic Analysis of A Nasp-Like Vertical Fin. *AIAA 33rd Structures, Structural Dynamics And Materials Conference*.

- Sakata, I.F., Davis, G.W. Robinson, J.C., Yates, E.C. (1975). Design Study of Structural Concepts for an Arrow-Wing Supersonic-Cruise Aircraft. *AIAA Aircraft Systems and technology Meeting*.
- Sani, A.S., Roohi, E., Kahrom, M., Stefanov, S. (2014). Investigation of Aerodynamic Characteristics of Rarefield Flow Around NACA 0012 airfoil using DMSC and NS Solvers. *European Journal of Mechanics/Fluids*.
- Sheldahl, R. E., Klimas, P. C. (1981). *Aerodynamic Characteristics of Seven. Symmetrical Airfoil Sections Through. 180-Degree Angle of Attack for Use in. Aerodynamic Analysis of Vertical Axis Wind Turbines*. Sandia National Laboratory.
- Sutherland, W. (1893). The viscosity of gases and molecular force. *Philosophical Magazine Series 5*, 507-531.
- Tamma, K.K., Thornton, E.A. (1984). Reentry Thermal-Structural Finite Element Analysis of Shuttle Wing Configurations. *22nd AIAA Aerospace Sciences Meeting*.
- Versteeg, H.K., Malalasekera W. (2007). *An Introduction to Computational Fluid Dynamics*. England: Pearson Prentice Hall.
- Wright, B.R., Bruckman, F., Radovcich, N.A. (1978). Arrow Wings for Supersonic Cruise Aircraft. *Journal of Aircraft*.

APPENDIX A

MATERIAL CHARACTERIZATION TESTS

The temperature difference affects the thermal and the mechanical properties of many materials. Elasticity is one of these properties and it is inversely proportional to the temperature and it decreases with increasing temperature. It is also dependent to the material type and the exposure time to the high temperature. The body deformation is related to the material elasticity. Therefore, the change in the elasticity must be determined before the simulations.

In the flight test conducted by the Langley Research Center, test sample was made of aluminum 2000 series. Thus, the change in the elasticity of aluminum 2000 series is needed in the finite element simulations carried out in this thesis work.

For aluminum 2000 series, the percent changes of the elastic properties are demonstrated in Figure 81 that shows that the exposure time is restricted by 1/2, 10, 100, 1000 and 10000 hours. These values are outside the time limit for many missile systems. There is no data set for the short exposure time; therefore, the high temperature tensile tests for the short exposure time (1 min) are conducted at the Atılım University Metal Forming Center of Excellence.

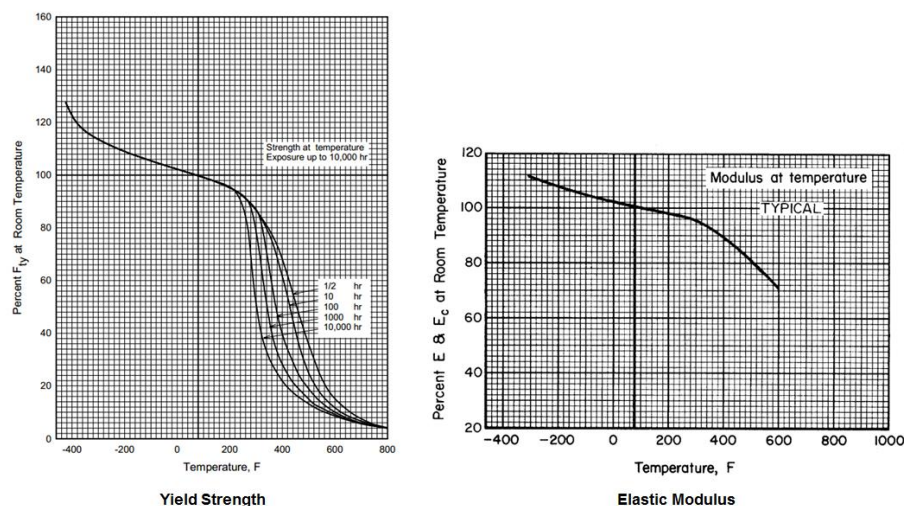


Figure 81. The percent change in elastic properties of Aluminum 2000 series

Tests are conducted with the tension/compression module (DIL805T) attached to the TA/Bähr DIL805A/D simulation system. This device is the module that has a heat and mechanic closed loop controller. The test setup and the test sample used in these test are demonstrated in Figure 82 and Figure 83.

During the test, the sample is heated only in the middle section ($\text{Ø}3 \times 5\text{mm}$) by an induction coil and the temperature at that location is controlled with an S-type thermocouple. The heating process is performed under the vacuum environment ($P=5 \times 10^{-4}$ mbar) in order to prevent the sample from being affected by the high temperatures.

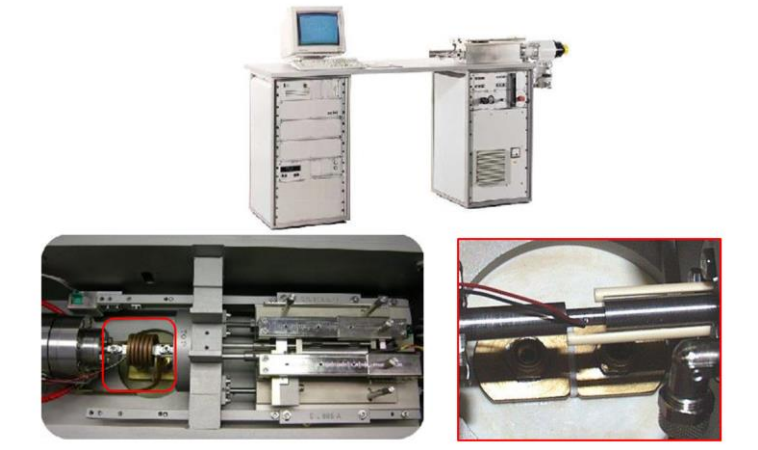


Figure 82. Test setup

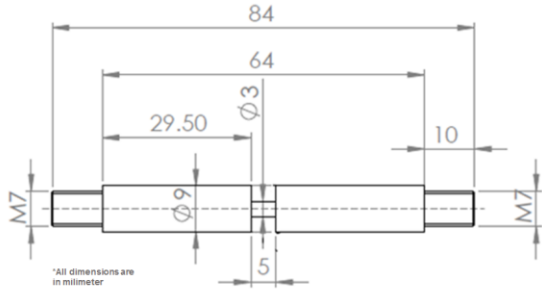


Figure 83. Test sample

In order to obtain the temperature dependent properties, tests are performed with four different temperature levels (25°C, 200°C, 250°C, 300°C). The stress-strain relations for these temperature levels are obtained and given from Figure 84 to Figure 87. The summary of these results are shown in Figure 88. According to the results, the

tensile strength of the material decreases by 30% for exposing to 300°C for 1 minute and the yield strength decreases more slowly than the tensile strength with increasing temperature.

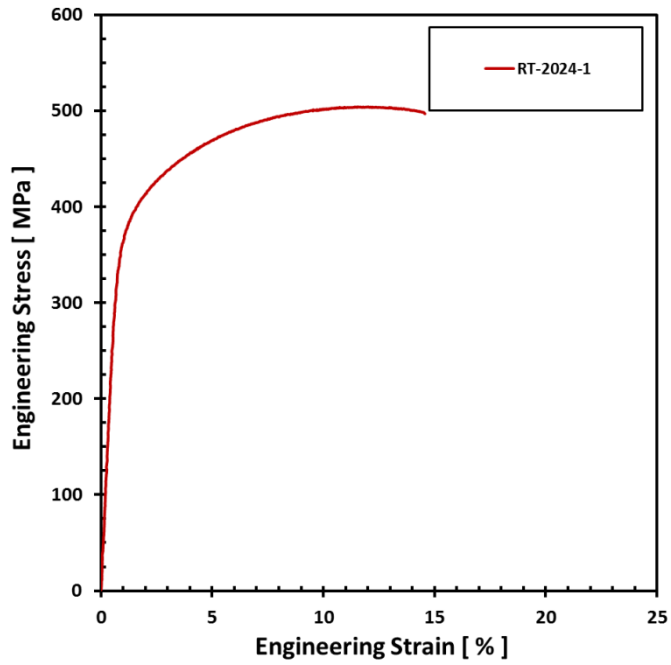


Figure 84. Stress-strain relation for 25°C

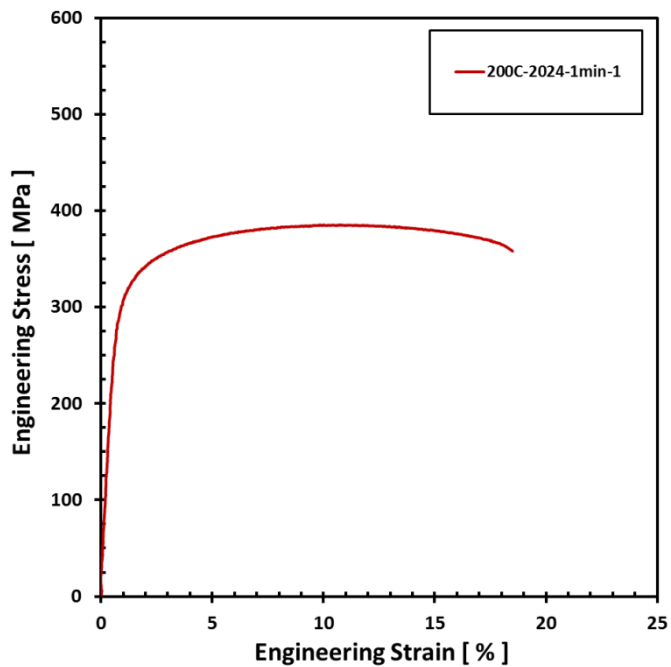


Figure 85. Stress-strain relation for 200°C

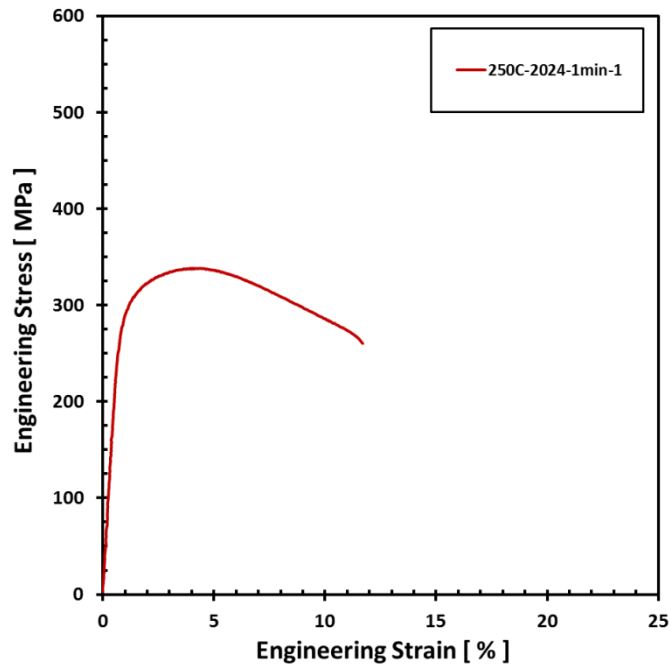


Figure 86. Stress-strain relation for 250°C

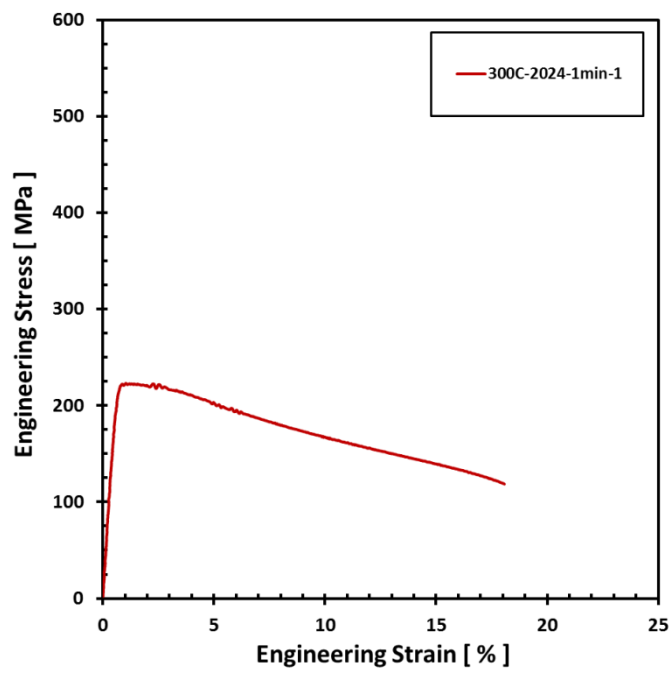


Figure 87. Stress-strain relation for 300°C

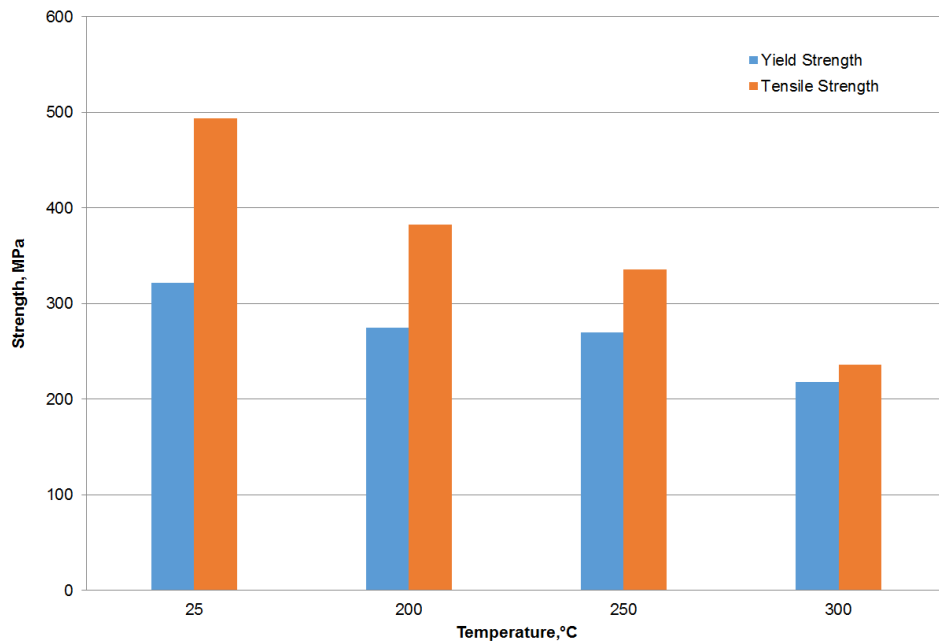


Figure 88. The change in the yield and the tensile strength with temperature

In order to obtain the elastic and the plastic data for each temperature level, the engineering stress and the engineering strain values given in figures converted to the true stress and the true strain values by using Equation 32 and Equation 33 from Callister (2007).

$$\sigma_T = \sigma_E(1 + \epsilon_E) \quad (32)$$

$$\epsilon_T = \ln(1 + \epsilon_E) \quad (33)$$

For each temperature levels, the elastic modulus could be obtained from the stress-strain graphs. The percent reduction of the elastic modulus with the exposed temperature is given in Figure 89.

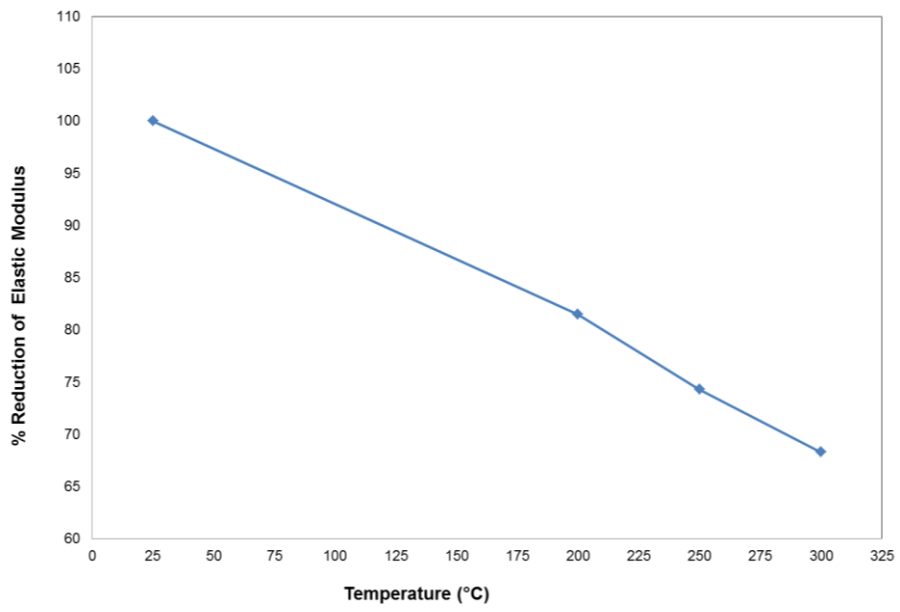


Figure 89. The percent reduction of elastic modulus with exposed temperature